Double-Hollow Au@CdS Yolk@Shell Nanostructures as Superior Plasmonic Photocatalysts for Solar Hydrogen Production

Yi-An Chen, Yuhi Nakayasu, Yu-Chang Lin, Jui-Cheng Kao, Kai-Chi Hsiao, Quang-Tuyen Le, Kao-Der Chang, Ming-Chung Wu, Jyh-Pin Chou, Chun-Wei Pao, Tso-Fu Mark Chang, Masato Sone, Chun-Yi Chen,* Yu-Chieh Lo,* Yan-Gu Lin,* Akira Yamakata,* and Yung-Jung Hsu*

Structural engineering has proven effective in tailoring the photocatalytic properties of semiconductor nanostructures. In this work, a sophisticated double-hollow yolk@shell nanostructure composed of a plasmonic, mobile, hollow Au nanosphere (HGN) yolk and a permeable, hollow CdS shell is proposed to achieve remarkable solar hydrogen production. The shell thickness of HGN@CdS is finely adjusted from 7.7, 18.4 to 24.5 nm to investigate its influence on the photocatalytic performance. Compared with pure HGN, pure CdS, a physical mixture of HGN and CdS, and a counterpart single-hollow cit-Au@CdS yolk@shell nanostructure, HGN@CdS exhibits superior hydrogen production under visible light illumination ($\lambda = 400–700$ nm). The apparent quantum yield of hydrogen production reaches 8.2% at 320 nm, 6.2% at 420 nm, and 4.4% at 660 nm. The plasmon-enhanced activity at 660 nm is exceptional, surpassing the plasmon-induced photoactivities of the state-of-the-art plasmonic photocatalysts ever reported. The superiority of HGN@CdS originates from the creation of charge separation state at HGN/CdS heterojunction, the considerably long-lived hot electrons of plasmonic HGN, the magnified electric field, and the advantageous features of double-hollow yolk@shell nanostructures. The findings can provide a guideline for the rational design of versatile double-hollow yolk@shell nanostructures for widespread photocatalytic applications.

1. Introduction

Solar hydrogen (H_2) fuel has sparked substantial interest over the past half century, as it has the potential to meet the growing global energy demand. This technology encounters the difficulty of low conversion efficiency due to the limited intrinsic properties of the photocatalyst materials. Light harvesting and utilization, charge transfer dynamics, and sufficient redox potentials for the desired reactions are the important properties that are highly related to photocatalytic efficiency. Nevertheless, it is impossible for a single material to meet all the requirements. To address these issues, modification of single materials by means of dopant introduction[1,2] and heterostructure formation[3] has been widely used. Among the different approaches, introducing metal@semiconductor heterojunctions has drawn especially important attention due to their several advantageous features. Upon excitation of a semiconductor, the metal can serve as a charge transfer mediator to improve the charge separation

Y.-A. Chen, J.-C. Kao, Q.-T. Le, Y.-C. Lo, Y.-J. Hsu
Department of Materials Science and Engineering
National Yang Ming Chiao Tung University
Hsinchu 300093, Taiwan
E-mail: yclo@nycu.edu.tw; yhsu@nycu.edu.tw

Y. Nakayasu, A. Yamakata
Graduate School of Natural Science and Technology
Okayama University
Okayama 700–8530, Japan
E-mail: yamakata@okayama-u.ac.jp

Y.-C. Lin, Y.-G. Lin
National Synchrotron Radiation Research Center
Hsinchu 30076, Taiwan
E-mail: lin.yg@nsrrc.org.tw

J.-C. Kao, C.-W. Pao
Research Center for Applied Sciences
Academia Sinica
Taipei 11529, Taiwan

K.-C. Hsiao, M.-C. Wu
Green Technology Research Center
Chang Gung University
Taoyuan 33302, Taiwan

**ADVANCED
SCIENCE NEWS**

www.advancedsciencenews.com

**ADVANCED
FUNCTIONAL
MATERIALS**

www.afm-journal.de

efficiency.[4–6] Thus, the carrier utilization efficiency can be increased to benefit the photocatalytic performance. On the other hand, plasmonic metal nanostructures, such as Au and Ag, possess a localized surface plasmon resonance (LSPR) effect,[7] which can be maneuvered to supplement the photon harvesting efficiency for semiconductors. In particular for Au, the possibility of tuning the plasmonic absorption toward the visible and even near infrared region has significant implications in photocatalytic applications.[8–10] Much research has utilized Au nanostructures as an alternative to traditional narrow-bandgap semiconductor photocatalysts in order to extend the photoactive range to visible and near infrared region.

Compared with solid Au, hollow Au nanospheres (HGN) have more flexible LSPR properties since both the inner and outer surfaces can contribute surface plasmons.[11,12] By adjusting the diameter to thickness ratio,[13–15] the LSPR wavelength of hollow Au can be shifted to a large extent, providing more tunability of the LSPR wavelength. Nevertheless, there are only a few studies on the development of HGN@semiconductor heterostructures for photocatalysis.[16,17] The synergy between HGN and semiconductors and its influence on the solar H_2 production efficiency has not been extensively explored. Owing to the proper band structure, CdS has been widely used in solar H_2 production.[18,19] However, its medium bandgap prohibits CdS from harvesting the solar spectrum at wavelengths beyond 550 nm. Through cooperation with HGN, the light harvesting range of CdS can be extended to cover the whole visible light region. Upon LSPR excitation, the plasmon energy of HGN can be transferred to CdS by hot electron injection and electrical field enhancement. This would enable CdS to generate additional charge carriers beyond bandgap excitation to contribute to solar H_2 production. In addition to the heterojunction introduction, structural engineering has long been regarded as one of the critical factors affecting the activity of photocatalysts. Configurations, such as particle-

K.-D. Chang
Mechanical and Systems Research Laboratories
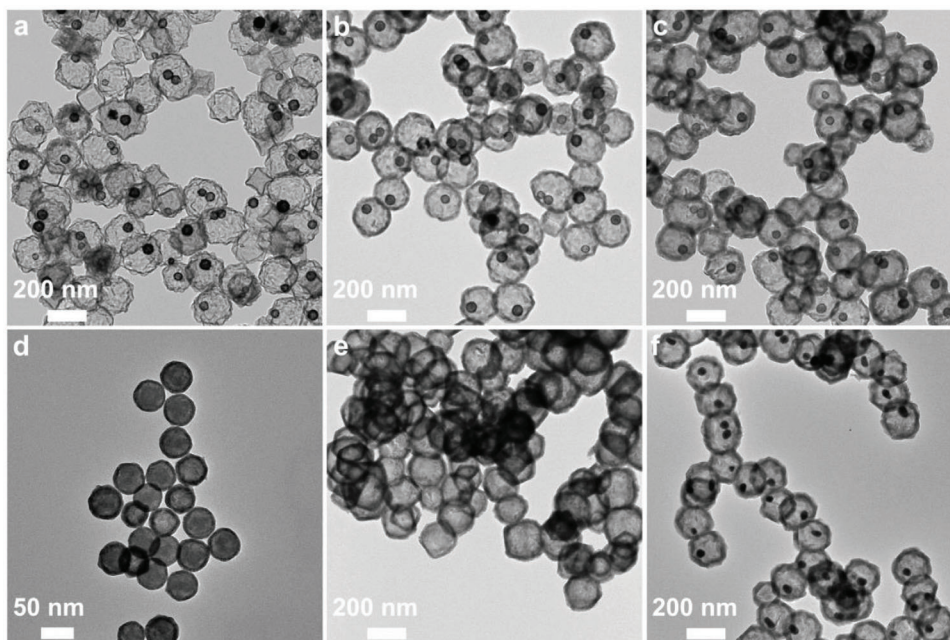Industrial Technology Research Institute
Hsinchu 31040, Taiwan

J.-P. Chou
Department of Physics
National Changhua University of Education
Changhua 50007, Taiwan

T.-F. M. Chang, M. Sone, C.-Y. Chen
Institute of Innovative Research
Tokyo Institute of Technology
Kanagawa 226–8503, Japan
E-mail: chen.c.ac@m.titech.ac.jp

Y.-J. Hsu
Center for Emergent Functional Matter Science
National Yang Ming Chiao Tung University
Hsinchu 300093, Taiwan

Y.-J. Hsu
International Research Frontiers Initiative
Institute of Innovative Research
Tokyo Institute of Technology
Kanagawa 226–8503, Japan

T.-F. M. Chang, M. Sone, C.-Y. Chen
Sumitomo Chemical Next-Generation Eco-Friendly Devices Collaborative
Research Cluster
Kanagawa 226-8503, Japan

decorated nanostructures,[20,21] Janus-like nanostructures,[22,23] core@shell[24,25] and yolk@shell nanostructures,[26–28] have provoked considerable attention. Being analogous to core@shell nanostructures, yolk@shell nanostructures hold many appealing microstructural features that can be utilized for photocatalytic applications.[29] Especially for metal@semiconductor yolk@shell nanostructures, the synergy between metal and semiconductor components can give rise to superior materials properties that can be exploited for promoting catalytic reactions.[28,30] In yolk@shell nanostructures, the catalytic process benefits significantly from the unique architecture where metal nanoparticles, often prone to aggregation and subsequent reduction in activity, are individually encased in protective shells. This encapsulation not only mitigates aggregation but also ensures long-term stability during operations. The shells, characterized by their permeability,[31,32] offer catalytic sites both internally and externally, thereby enhancing the efficiency of catalytic reactions. The hollow interior within these shells serves as a nanoreactor, facilitating the diffusion of reactants and products, which further amplifies the overall catalytic performance. Additionally, the mobility of the encapsulated yolk particles within the shell acts as a micro-stirrer, dynamically enhancing the reaction kinetics. Previous studies have examined the mobility of yolk particles in the yolk@shell nanostructures by real-time electronic spectroscopy.[26,33] This stirring effect not only promotes more efficient mixing of the reaction contents but also contributes to the accelerated catalytic activity, leveraging the full potential of the yolk@shell structure in catalysis. In addition to their intriguing microstructural features, yolk@shell nanostructures can also be engineered to exhibit superior optical properties compared to traditional core@shell nanostructures. For metal@semiconductor yolk@shell nanostructures, one side of the metal yolk is in direct contact with the semiconductor shell, while the opposite side faces the surrounding medium. This asymmetric interface between the metal yolk and the semiconductor shell leads to the pronounced localization of electric near-fields, thereby enhancing optical absorption and facilitating charge separation.[34] Due to these tailored optical properties, yolk@shell nanostructures may demonstrate exceptional promise in photocatalytic applications, surpassing the performance of core@shell nanostructures.

For photocatalytic applications, the structural parameters of photocatalysts are of paramount significance and should be rationally engineered. For yolk@shell nanostructures, the void size has been demonstrated to be a decisive factor in optimizing the solar H_2 production activity since mass transport kinetics can be largely affected by this factor.[35] On the other hand, it has been reported that the shell thickness of hollow nanostructures affects the photocatalytic performance by mediating light scattering, charge transport distance and band structure. Zou et al. found that TiO_2 microtubes with a suitable shell thickness can perfectly balance light absorption capability and charge separation efficiency, achieving an optimized photocatalytic activity for dye degradation.[36] Wang et al. reported that the thinner shell thickness of covalent triazine frameworks in hollow sphere morphology was endowed with a more negative conduction band edge, which is beneficial for charge separation and thus H_2 production.[37] However, this factor has never been examined in yolk@shell nanostructures. In this work, we synthesized HGN@CdS yolk@shell nanostructures with controllable shell

**ADVANCED
SCIENCE NEWS**

www.advancedsciencenews.com

**ADVANCED
FUNCTIONAL
MATERIALS**

www.afm-journal.de

Figure 1. TEM images of a) HGN@CdS-1, b) HGN@CdS-2, c) HGN@CdS-3, d) pure HGN, e) pure CdS, f) cit-Au@CdS.

thicknesses from 7.7, 18.4, to 24.5 nm and investigated the effect of the shell thickness on the solar H_2 production. An optimal thickness of 18.4 nm for maximizing the solar H_2 production activity was observed. Compared with the relevant samples, including pure HGN, pure CdS, a physical mixture of HGN and CdS, and a counterpart single-hollow cit-Au@CdS yolk@shell nanostructure, HGN@CdS exhibited superior H_2 production under visible light illumination ($\lambda = 400–700$ nm), achieving an apparent quantum yield of H_2 production of 8.2% at 320 nm, 6.2% at 420 nm, and 4.4% at 660 nm. The superiority of HGN@CdS originated from the creation of charge separation state at HGN/CdS heterojunction, the considerably long-lived hot electrons of plasmonic HGN, the magnified electric field, and the advantageous features of double-hollow yolk@shell nanostructures.

2. Results and Discussion

2.1. Microstructural Features and Optical Properties

The sacrificial template is a common technique used to synthesize hollow structures. In this work, Co_xB_y scaffolds and Cu_2O served as templates for HGN and hollow Cu_7S_4, respectively. Co-based particles are vulnerable to oxidation and are commonly used for hollow structure fabrication[38] due to the considerably negative reduction potential of Co^{2+}/Co ($E_0 = −0.277$ V *vs* SHE).[39] As the Co_xB_y scaffolds were exposed to $HAuCl_4$, Au started to deposit on the surface of Co_xB_y through galvanic replacement because of the higher standard reduction potential of $AuCl_4^-$ ($AuCl_4^-/Au$, $E_0 = 0.994$ V versus SHE)[40] than Co^{2+}/Co, forming Co_xB_y@Au core@shell nanostructures. Afterward, the residual Co_xB_y core was oxidatively etched by air, leaving only the external Au shell. On the other hand, because of the difference in solubility between Cu_2O ($K_{sp} = 2 \times 10^{-15}$) and Cu_7S_4 ($K_{sp} = 1 \times 10^{-48}$),[41,42] Cu_2O can be spontaneously transformed into Cu_7S_4

once Na_2S is introduced. Additionally, because the S^{2-} ions diffused more slowly inward than the Cu^{2+} ions diffused outward, a void space formed between Cu_2O and Cu_7S_4. This nanoscale Kirkendall effect[43] accounted for the formation of hollow Cu_7S_4.

HGN@CdS with the double-hollow architecture was clearly distinguished, as shown in **Figure 1a–c**. The shell thickness of CdS was modified to 7.7 ± 1.8, 18.4 ± 2.9 and 24.5 ± 3.3 nm for HGN@CdS-1, HGN@CdS-2 and HGN@CdS-3, respectively, while the void sizes in the three HGN@CdS were nearly identical, around 160.1 ± 10.1, 160.1 ± 8.7, and 163.7 ± 10.5 nm. This enabled the independent investigation of the effect of the CdS shell thickness. Pure HGN comprised a hollow spherical morphology with a void size of 41.8 ± 4.0 nm and a shell thickness of 5.7 ± 1.5 nm. The hollow structure of pure CdS could also be observed in Figure 1e, with the void size (165.9 ± 29.5 nm) and shell thickness (19.0 ± 3.8 nm) approximating those of HGN@CdS-2. As a counterpart single-hollow yolk@shell nanostructure, in which only shell is hollow, the synthesis of cit-Au@CdS employed solid citrate-protected Au (cit-Au) nanoparticles as core. The Au size and CdS shell thickness of cit-Au@CdS was 43.63 ± 5.79 nm and 21.6 ± 3.0 nm, respectively. Instead of controlling the shell thickness, the Au/CdS molar ratio of cit-Au@CdS was adjusted to equal the composition of HGN@CdS-2. With this operation, the possible composition effect can be ruled out. Therefore, the performance comparison between HGN@CdS-2 and cit-Au@CdS could highlight the beneficial features of the double-hollow structure for HGN@CdS. As observed from the transmission electron microscopy (TEM) images, the HGN yolks were randomly located in the interior of the CdS shell, indicating that HGN could freely move inside the CdS. In this situation, the surface active sites of HGN were maximally exposed, which could benefit the photocatalytic performance. The microstructure and composition of HGN@CdS were further inspected by high-resolution TEM (HRTEM), selected-area electron
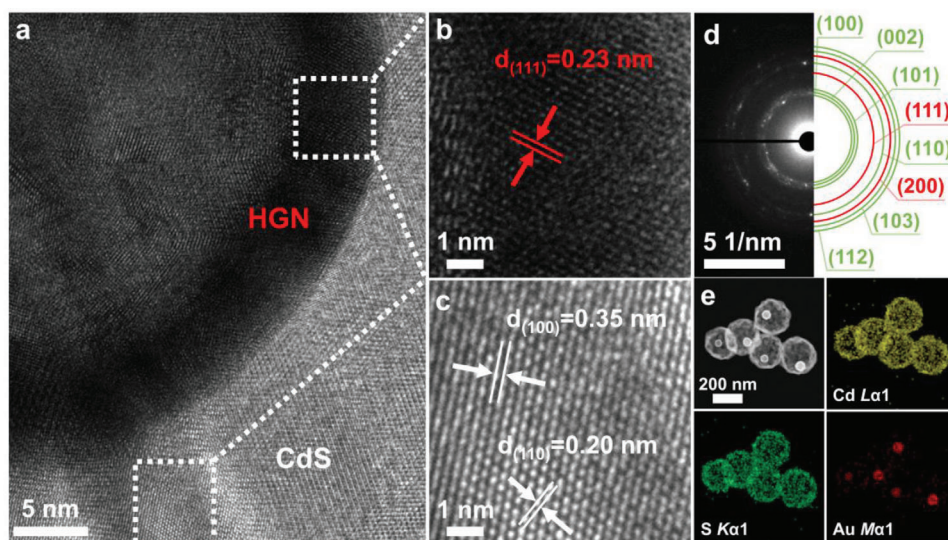
Figure 2. a–c) HRTEM images, d) SAED pattern, e) HADDF image and the corresponding TEM-EDS mapping data for HGN@CdS.

diffraction (SAED), high-angle annular dark-field imaging (HAADF), and TEM energy-dispersive X-ray spectroscopy (TEM-EDS) analysis. As shown in **Figure** 2a–c, the higher contrast region had a lattice spacing of 0.23 nm, which was assigned to the (111) plane of fcc Au. The lower contrast region had lattice spacings of 0.35 and 0.20 nm, corresponding to the (100) and (110) planes of wurtzite CdS, respectively. In Figure 2d, a set of CdS and Au characteristic planes were verified from the SAED pattern. The HAADF image and EDS mapping data in Figure 2e further showed that Au was present inside the structure, while Cd and S were distributed across the entire structure, confirming the yolk@shell structural features for HGN@CdS. Inductively coupled plasma-mass spectrometry (ICP-MS) analysis was conducted to ascertain the elemental composition of Au, Cd, and S for HGN@CdS. The analytical data, detailed in Table S1 (Supporting Information), revealed a congruence between the experimentally measured contents and the theoretical values, which were derived based on microstructural data. For example for HGN@CdS-2, the measured weight percentages of Au, Cd, and S were 9.5%, 73.4% and 17.1%, respectively. These experimentally measured values aligned with the theoretically calculated percentages, which were anticipated to be 8.8% for Au, 71.0% for Cd, and 20.2% for S. This alignment not only corroborates the accuracy of the calculations but also reinforces the reliability of the structural characterization of HGN@CdS.

The optical properties were analyzed with UV–vis absorption and diffuse reflectance spectroscopy (DRS). The extinction spectra of the relevant samples are displayed in Figure S1a (Supporting Information). The LSPR absorption of pure HGN and cit-Au was observed at 607 and 532 nm, respectively. These values were consistent with those reported for hollow Au[44] and cit-Au.[45] Pure CdS exhibited strong absorption with a peak located at 500 nm, which was attributed to band edge absorption. For HGN@CdS, a prominent absorption peak ascribable to the band edge absorption of CdS was still observed. An additional shoulder appeared at approximately 650 nm, which was caused by the LSPR of the HGN yolk. These spectral features

were more clearly identified in the DRS spectra. As shown in Figure S2 (Supporting Information), apparent LSPR absorption peaks located at 580, 586, 648, 650 and 590 nm were observed for pure HGN, HGN@CdS-1, HGN@CdS-2, HGN@CdS-3 and cit-Au@CdS, respectively. According to Mie theory, the refractive index of the surrounding medium greatly affects the absorption characteristics of dispersing particles. For plasmonic nanoparticles, increasing the refractive index of the surrounding medium results in a redshifted response. For the current HGN@CdS, the larger refractive index of CdS (n = 2.19–2.52)[46] than that of the solvent (water, n = 1.33) led to the redshift of the LSPR band relative to pure HGN. As the volume fraction of the shell increased, the impact of the shell layer on the HGN yolk became more prevalent, causing the plasmon band to substantially shift to a longer wavelength.[47] As shown in Figure S1a (Supporting Information), the distinct solution colors of the suspension among the three HGN@CdS samples also reflected this difference. The corresponding XRD patterns are displayed in Figure S1b (Supporting Information). The typical diffraction peaks of wurtzite CdS and fcc Au were verified. The characteristic peaks of Cu_7S_4 were not observed, indicating that Cu^{2+} was completely replaced by Cd^{2+} in the cation exchange process.
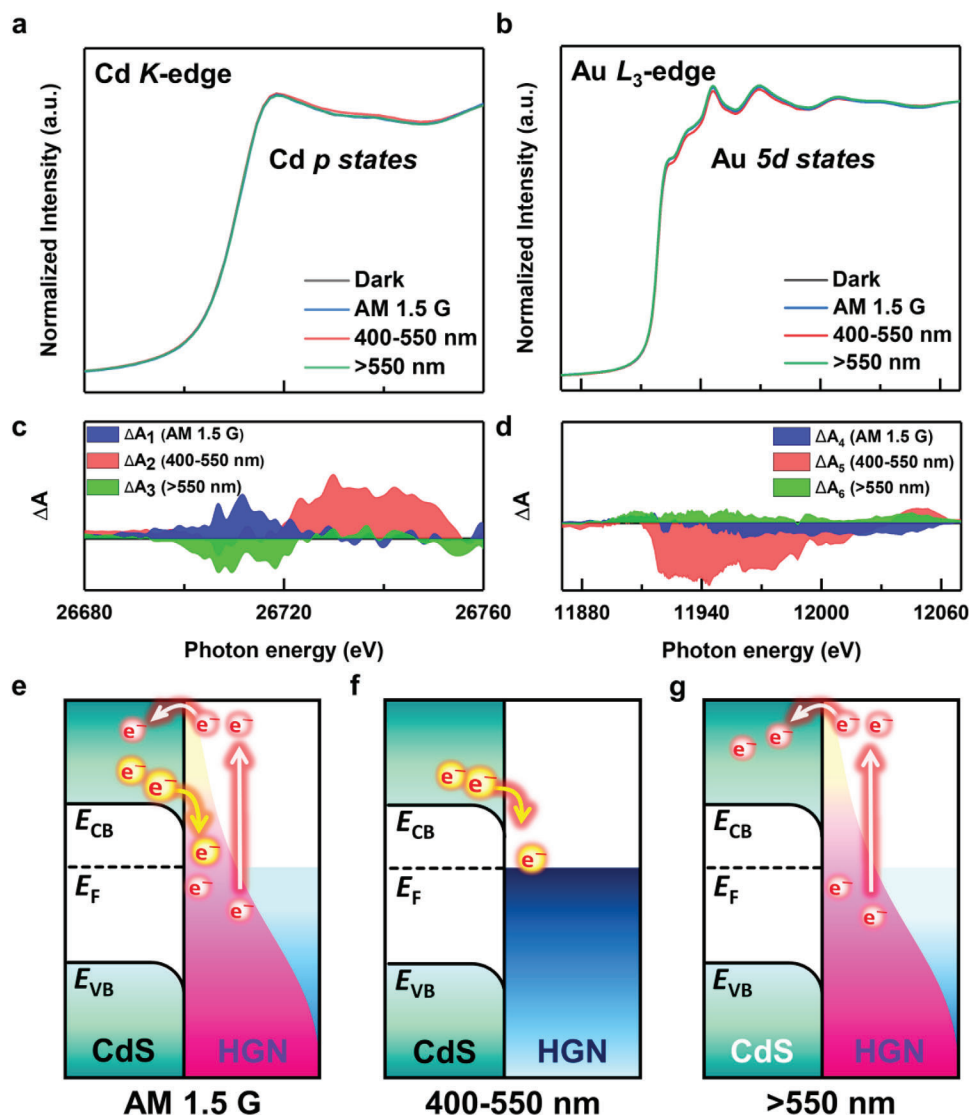
2.2. Band Structure and Band Alignment

Determination of the electronic band structure is necessary to understand the charge transfer pathways at the interfaces. From Figure S3a (Supporting Information), the ultraviolet photoelectron spectroscopy (UPS) spectra for pure CdS and pure HGN showed sharp cutoff edges at 16.60 and 17.34 eV, respectively. The work function could be calculated by subtracting the cutoff energy from the excitation energy (hv = 21.22 eV for He I); the work function for CdS and HGN was determined to 4.62 and 3.88 eV, respectively. The valence band maximum (E_{VB}) with respect to the Fermi level (E_F) could be determined by the intersection of linear extrapolation along the onset edge and the extended baseline of

the spectrum. As shown in Figure S3b (Supporting Information), the E_{VB} of pure CdS was determined to be 1.52 eV with respect to E_F. The Tauc plot in Figure S3c (Supporting Information) showed that the optical bandgap of pure CdS was 2.38 eV. The conduction band minimum (E_{CB}) of pure CdS could be further determined by subtracting the E_{VB} from the bandgap. Accordingly, a complete band structure was constructed in Figure S3d (Supporting Information). Before contact, the E_F of pure CdS and pure HGN was −4.62 and −3.88 eV versus vacuum, respectively. The E_{CB} and E_{VB} of CdS were located at −3.76 and −6.14 eV versus vacuum, respectively. As HGN was put in contact with CdS, band alignment occurred, leading to downward bending of the CdS band edge at the HGN/CdS interface. This band alignment may further steer the dynamics of the photoexcited charge carriers of CdS. Upon bandgap excitation, the downward band bending at the interface can facilitate photoexcited electron transfer from CdS to HGN and enable the photogenerated holes to be concentrated in CdS. Because the photoexcited electrons were separated from the photogenerated holes, radiative electron-hole recombination could be reduced to cause a depressed PL intensity for HGN@CdS. As displayed in Figure S3e (Supporting Information), HGN@CdS exhibited noticeable PL quenching relative to pure CdS, validating that the radiative recombination of CdS was effectively retarded by the presence of HGN.

To further clarify the charge transfer pathway under bandgap excitation, the photo-Kelvin probe force microscopy (KPFM) measurements were performed. The samples were drop-cast on the silicon substrate for measurement. The surface topographic image for HGN@CdS and the resultant surface potential images recorded in the dark and under light illumination are shown in Figure S4a–c (Supporting Information). Note that UV-B irradiation (λ = 312 nm) was employed to exclusively excite CdS, enabling the observation on the behavior of the photoexcited electrons of CdS. To examine how the surface potential difference (ΔSP) changes with yolk@shell nanostructure formation, pure HGN and pure CdS were also analyzed, and the results are shown in Figure S5 (Supporting Information). Figure S4d (Supporting Information) summarizes the ΔSP of the three samples between irradiation and dark conditions. Here, a negative ΔSP corresponds to the generation of photoexcited electrons and their accumulation in the sample, causing an increased electron density. In contrast, a positive ΔSP signifies the depletion of the electron density. Under dark condition, the surface potential of pure HGN was measured to be 5.162 V, whereas under illumination, the surface potential shifted to 5.155 V. A negative ΔSP of -7 mV was noted for pure HGN, suggesting that some photoexcited electrons from silicon substrate were transported and accumulate in HGN after light illumination. For pure CdS, an immediate increase in surface potential from 4.907 to 4.913 V was observed upon irradiation (ΔSP = 6 mV). This phenomenon suggested that the photoexcited electrons of CdS transferred to the silicon substrate. For HGN@CdS, a dramatic decrease in surface potential from 4.993 to 4.972 V was noticed after light illumination (ΔSP = −21 mV), reflecting a considerable increase in overall electron density. Owing to the band alignment at HGN/CdS interface, the photoexcited electrons of CdS would preferentially transfer and remain in HGN. This caused a considerable increase in overall electron density to result in the greatly negative ΔSP observed for HGN@CdS.

2.3. Charge Transfer Mechanism and Dynamics

X-ray Absorption Spectroscopy (XAS) was further utilized to investigate the charge transfer mechanism in HGN@CdS under light illumination. By comparing the XAS spectral intensities of selected atoms between darkness and irradiation conditions, variations in the unoccupied density of states (UDOS) due to irradiation can be determined. These spectroscopic data provide both qualitative and quantitative insights, enabling the identification of the pathway and number of charge carriers that are transported under light illumination.[48–50] In **Figure 3a**, the Cd K-edge X-ray absorption near edge structure (XANES) spectra of HGN@CdS under darkness and irradiation conditions showed characteristic features of CdS.[51,52] The prominent absorption peak at approximately 26 718 eV with a mild shoulder at 26 737 eV were associated with core electron excitation from Cd $1s$ to unoccupied $5p$ orbitals. Figure 3b illustrates the feature of the Au L_3-edge XANES spectra for HGN@CdS, revealing typical fcc structure of Au with three prominent peaks observed in the 11 900–11 980 eV range.[50,53] These peaks involved dipole transitions from $2p_{3/2}$ and $2p_{1/2}$ to $5d$. Further spectral comparison for the data collected in the dark with those collected under irradiation conditions was performed, and the results were illustrated in Figure 3c,d. Under AM 1.5 G illumination, the intensity of the Cd K-edge spectrum of HGN@CdS was increased, showing a positive intensity difference spectrum ($\Delta A = A_{AM\ 1.5\ G} − A_{dark}$). The area under the ΔA spectrum (ΔA_1) was estimated to be 0.40. The increment in the XAS intensity reflected an increased UDOS for CdS, indicating the prevalence of electron transfer from CdS to HGN. As a complement, the intensity of the Au L_3-edge spectrum of HGN@CdS was decreased upon AM 1.5 G irradiation, exhibiting an negative ΔA_4 of −0.26. The pronounced electron accumulation in HGN may account for the observed intensity decrease of Au L_3-edge spectrum. Note that AM 1.5 G illumination can induce both band edge excitation of CdS and plasmonic excitation of HGN within HGN@CdS. Possible charge transfer scenarios included the transportation of the photoexcited electrons of CdS to HGN and the injection of hot electrons of plasmonic HGN into CdS. As displayed in Figure 3e, the two pathways may operate together to result in the increased UDOS for CdS component and the decreased UDOS for HGN component. This consideration was valid provided that the band edge excitation of CdS was predominant over the plasmonic excitation of HGN. To verify the contention, spectral comparison between darkness condition and visible irradiation was further performed in order to decouple the two pathways. In the comparative experiments, a bandpass filter (λ = 400–550 nm) was first placed over AM 1.5 G illumination to generate visible irradiation that can exclusively excite CdS component. Similar quantitative results were observed in the ΔA spectra, with the Cd K-edge spectrum showing a positive ΔA_2 of 0.60 and the Au L_3-edge spectrum showing a negative ΔA_5 of −1.23. As Figure 3f illustrates, under band edge excitation, the photoexcited electrons of CdS were transported to HGN. The comparative experiment was further performed by employing a long pass filter (λ > 550 nm) to enable the exclusive excitation of plasmonic HGN. Opposite spectral features were observed in the ΔA spectra, with the Cd K-edge spectrum showing a negative ΔA_3 of −0.13 and the Au L_3-edge spectrum showing a positive ΔA_6 of 0.36. Under plasmonic

**ADVANCED
SCIENCE NEWS**

www.advancedsciencenews.com

**ADVANCED
FUNCTIONAL
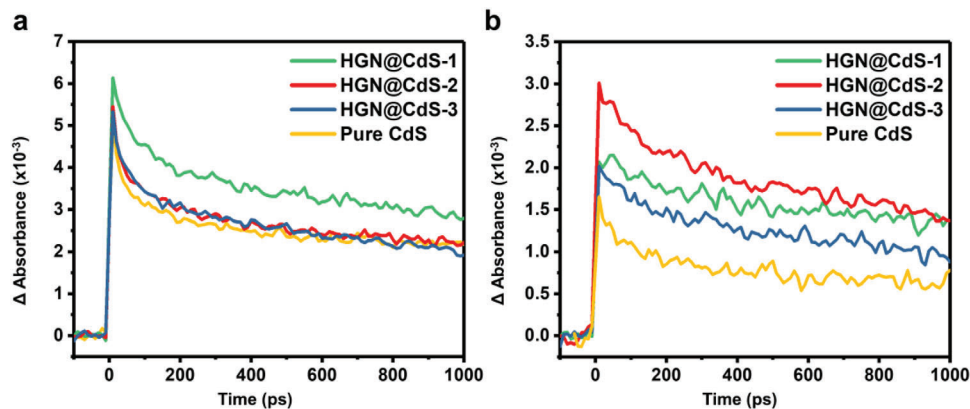MATERIALS**

www.afm-journal.de

Figure 3. XAS spectra of HGN@CdS recorded under darkness and irradiation conditions: a) Cd K-edge spectra and c) the corresponding intensity difference spectra, b) Au L_3-edge spectra and d) the corresponding intensity difference spectra. Proposed charge transfer scenarios for HGN@CdS under e) AM 1.5 G illumination, f) band edge excitation, g) plasmonic excitation.

excitation, hot electrons generated at HGN can be injected into CdS. As displayed in Figure 3g, since CdS received hot electrons from HGN, the UDOS of CdS was reduced to give rise to a negative ΔA_3.

It is important to notice that $|\Delta A_2|$ (0.60) was substantially larger than $|\Delta A_3|$ (0.13), and $|\Delta A_5|$ (1.23) was essentially larger than $|\Delta A_6|$ (0.36). This observation reflected that the effectiveness of band edge excitation of CdS in decreasing the UDOS of CdS was more pronounced than that of plasmonic excitation of HGN in increasing the UDOS of CdS. The collective operation of the two excitations under AM 1.5 G illumination can therefore compromise the extent of overall electron depletion for CdS component. This explained why AM 1.5 G illumination gave rise to a less extent of UDOS decrease of CdS component than 400–550 nm irradiation did for the current HGN@CdS. The compromised electron depletion for CdS under AM 1.5 G illumina-

tion, however, did not indicate the reduced number of the photoexcited electrons extracted from CdS. Since the two excitations occurred at different wavelength regions, i.e., band edge excitation of CdS at $\lambda < 550$ nm and plasmonic excitation of HGN at $\lambda > 550$ nm, they can jointly operate to promote the overall carrier utilization efficiency of CdS. For band edge excitation, the photoexcited electrons of CdS were transported to HGN through the HGN/CdS heterojunction. The separated electrons and holes can therefore survive for a sufficient time for participation in the subsequent redox reactions. On the other hand, for plasmonic excitation, the hot electrons of HGN were injected into CdS via the HGN/CdS heterojunction. These delocalized hot electrons rendered CdS with additional charge carriers, which can be utilized to conduct redox reactions as well. Such a sensitization effect can extend the photoactive region of CdS to a wavelength beyond band edge absorption. Note that the evolution of

**ADVANCED
SCIENCE NEWS**

www.advancedsciencenews.com
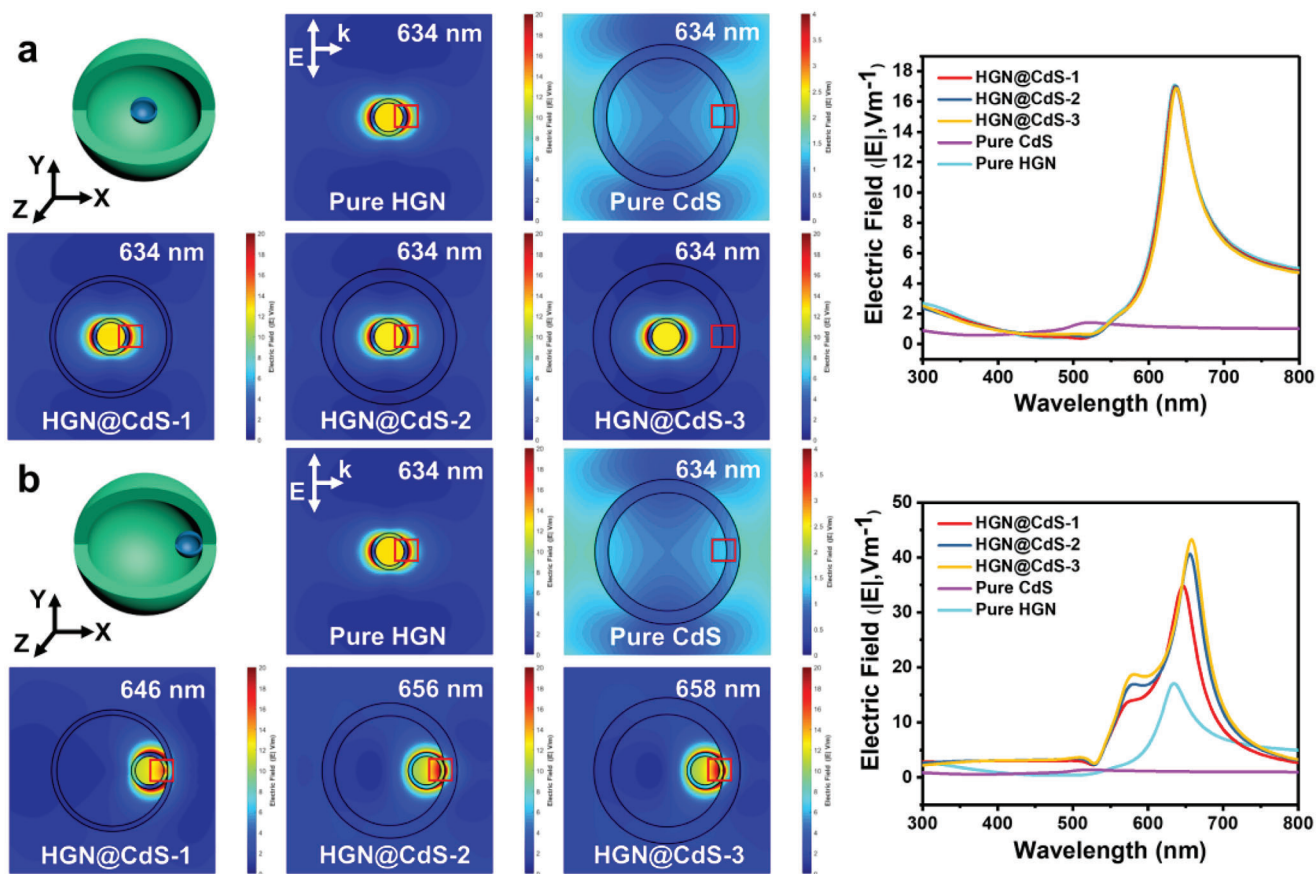
**ADVANCED
FUNCTIONAL
MATERIALS**

www.afm-journal.de

Figure 4. a) Kinetics traces probed at 650 nm for pure CdS and three HGN@CdS. The pump wavelength was 370 nm. b) Kinetics traces probed at 800 nm for pure CdS and three HGN@CdS. The pump wavelength was 560 nm for HGN@CdS-1 and 650 nm for other samples.

UDOS for HGN@CdS with light irradiation originated from the prevalence of interfacial charge transfer at the HGN/CdS heterojunction. Without this heterojunction, the photoexcited charge carriers and plasmonic hot electrons were prone to rapid charge recombination and relaxation. An invariant UDOS would be anticipated. Figure S6 (Supporting Information) further shows the Cd K-edge XANES spectra for pure CdS under darkness and irradiation conditions. No appreciate change in spectral intensity can be observed upon light irradiation, suggesting that the UDOS of pure CdS was unaffected by light irradiation. These comparative data confirmed the validness of the interpretations of XAS data for identifying the mechanism of interfacial charge transfer for the current HGN@CdS.

According to the XAS analytic results, two primary charge transfer scenarios may exist in HGN@CdS under light illumination, which can be maneuvered to tailor the photocatalytic properties. One was the band edge excitation of CdS, in which the photoexcited electrons of CdS would favorably transfer to HGN to result in spatial separation of electrons and holes. The other was associated with the plasmonic excitation of HGN and the subsequent relaxation of hot carriers. In order to explore the dynamics of these charge carriers, transient absorption (TA) measurements were conducted under two different pump wavelengths. The measurements were first carried out at a pump wavelength of 370 nm to interrogate the charge transfer dynamics associated with the band edge excitation of CdS. The TA profiles probed from 500 to 1000 nm at various delay times are shown in Figure S7 (Supporting Information). Both pure CdS and HGN@CdS exhibited noticeable photoinduced absorption signals across the probed wavelength region, suggesting the photoexcited electrons and holes were trapped upon band edge excitation. To identify the signals of the kinetics for the trapped electrons and holes in CdS, the TA profiles of pure CdS and HGN@CdS at 30–50 ps delay time were further compared. As highlighted in Figure S8 (Supporting Information), upon 370 nm excitation, HGN@CdS exhibited an increment of TA intensity from 580 to 750 nm as compared to pure CdS. As HGN can capture photoexcited electrons from CdS, the photogenerated holes can reside at CdS to result in the increased TA intensity for HGN@CdS. The TA signal at 650 nm can be therefore assigned to the trapped holes of CdS. On the other hand, the TA intensity

of HGN@CdS was reduced beyond 750 nm in relative to pure CdS. As the photoexcited electrons were extracted from CdS, a decreased TA intensity would be expected for HGN@CdS. In this regard, the TA signal at 800 nm can reflect the fate of the trapped electrons of CdS. The kinetics traces at the probe wavelength of 650 nm were further analyzed to investigate the fate of the trapped holes of CdS.[54] As shown in **Figure 4a**, pure CdS underwent a rapid decay of trapped holes kinetics with bi-exponential lifetime components of $\tau_1 = 22.9$ ps and $\tau_2 = 277$ ps, signifying the fast electron-hole recombination. The three HGN@CdS, on the other hand, exhibited prolonged decay kinetics of trapped holes, reflecting the creation of a charge separation state at the HGN/CdS heterojunction. The estimated bi-exponential lifetime components were $\tau_1 = 72.3$ ps and $\tau_2 = 1740$ ps, $\tau_1 = 29.6$ ps and $\tau_2 = 342$ ps, and $\tau_1 = 52.3$ ps and $\tau_2 = 1050$ ps for HGN@CdS-1, HGN@CdS-2 and HGN@CdS-3, respectively. This outcome was in consistence with the proposed scenarios of interfacial charge transfer for HGN@CdS in Figure 3f. Under band edge excitation, the delocalized electrons of CdS would be favorably transported to HGN. The trapped holes at CdS can thereby survive for an extended time to prolong the decay kinetics.

The charge transfer dynamics related to plasmonic excitation of HGN were further monitored by conducting the TA measurements at a designated pump wavelength that could excite the LSPR of HGN, i.e., 560 nm for HGN@CdS-1, 650 nm for HGN@CdS-2 and HGN@CdS-3, as estimated according to the absorption spectra. Pure CdS was also analyzed by TA using a pump wavelength of 650 nm to offer a comparative basis. Note that for CdS component, pumping at 650 nm could also induce sub-bandgap electronic transition due to the existence of defect states. In this regard, both sub-bandgap electronic transition and plasmonic excitation were involved in HGN@CdS. As displayed in Figure S9 (Supporting Information), all the samples were characteristic of a photoinduced absorption decay. This feature again implied the emergence of electron and hole trapping upon the plasmonic excitation. The decay profiles at 800 nm were further studied to deliver kinetics information for the trapped electrons of CdS. As compared in Figure 4b, the three HNG@CdS all exhibited prolonged decay kinetics than pure CdS did. The computed single-exponential lifetime was 216,

**ADVANCED
SCIENCE NEWS**

www.advancedsciencenews.com

**ADVANCED
FUNCTIONAL
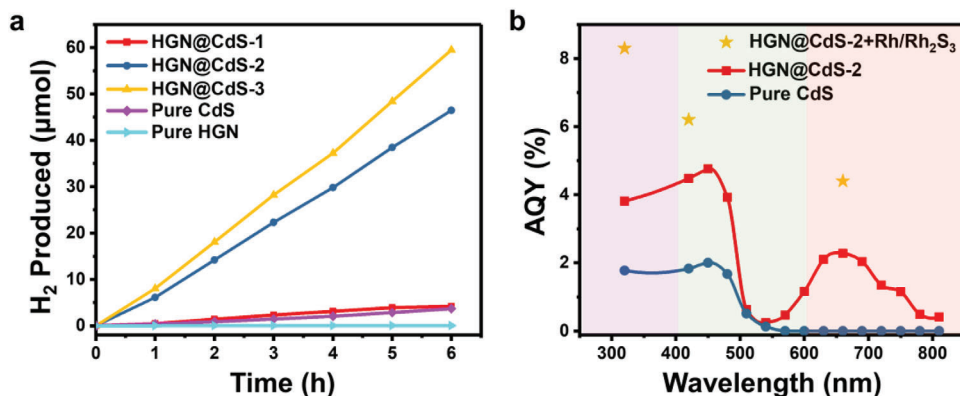MATERIALS**

www.afm-journal.de

Figure 5. Spatial distribution of simulated electric field distribution under an incident light of the indicated wavelength for pure HGN, pure CdS, and the three HGN@CdS. The modeled conditions included a) HGN situated at the center of CdS shell, b) HGN situated at the corner of CdS shell. The accumulative electric field along the x-y plane as a function of the incident wavelength at the marked region were also presented.

318, 330, and 337 ps for pure CdS, HGN@CdS-1, HGN@CdS-2 and HGN@CdS-3, respectively. The generation of hot electrons from the plasmonic HGN followed by their injection into CdS may account for the prolonged lifetime of the trapped electrons for the three HNG@CdS. Compared to other plasmonic systems based on Au-loaded semiconductor photocatalysts,[55–58] which usually showed an electron lifetime of a few ps to several tens of ps, the delocalized hot electrons in the current HGN@CdS were much more long-lived, which may guarantee its efficient photocatalytic performance under plasmonic excitation. In addition to the prolonged electron lifetime, the incremental number of delocalized electrons at CdS was also evident for the three HGN@CdS. As can be recognized from the intensity rise upon pumping, the substantially higher intensity of three HGN@CdS than pure CdS confirmed that a large number of hot electrons were injected into CdS upon plasmonic excitation.

Besides hot electron injection, localized electric field magnification can also be induced upon plasmonic excitation. This effect has proven pivotal in promoting charge generation and separation in plasmonic photocatalysts.[10,59] To assess the localized electric field of HGN@CdS and its implications on photocatalysis, finite-difference time-domain (FDTD) simulations were conducted. Eight representative conditions, including pure HGN, pure CdS and the three HGN@CdS with two distinct cases, were

modeled and compared. Here, two distinct cases of HGN@CdS were considered in order to account for the mobility of HGN and thus its random location within the CdS shell: i) HGN was located at the center spot of the CdS shell; ii) HGN was attached on the side spot of the CdS shell. **Figure 5** summarizes the accumulative electric field along the x-y plane as a function of incident wavelength at the marked region for the eight modeled conditions. Pure, isolated HGN showed a peaked electric field at 634 nm with an intensity of approximately 17.0 V m⁻¹. Notably, the inner surface of HGN also showed an intense electric field, suggesting that photons can be localized at the interior space. This feature further implied that light trapping in HGN could be more pronounced than that in solid cit-Au, which is beneficial for harvesting more photons. On the other hand, pure CdS displayed an electric field distribution associated with the excitonic absorption feature, comprising a peak intensity of 1.4 V m⁻¹ at 522 nm. For HGN@CdS, the case with HGN situated at the center displayed negligible change in electric field distribution. This outcome was expectable because HGN was not in contact with CdS. For the case with HGN situated at the corner, the simulation results showed an obvious shift of electric field with increasing shell thickness. The direct contact of HGN with CdS can modify the dielectric of the surrounding environment, leading to the significant frequency change in the localized electric field. Furthermore, the electric field intensity of HGN@CdS was

ADVANCED
SCIENCE NEWS

www.advancedsciencenews.com

ADVANCED
FUNCTIONAL
MATERIALS

www.afm-journal.de

Figure 6. a) Comparative results of photocatalytic H_2 production over relevant samples. b) Wavelength-dependent AQY spectra of pure CdS, HGN@CdS-2 and HGN@CdS-2 loaded with Rh/Rh$_2$S$_3$ co-catalyst.

gradually elevated with shell thickness. This phenomenon can be understood by the reduced curvature of the CdS shell with increasing thickness. It was reported that a smaller curvature could reduce light momentum dispersion and further promote the oscillation of surface plasmons,[60] thus giving rise to a more intense electric field. A peak intensity of 34.8 V m^{-1} at 646 nm, 40.6 V m^{-1} at 656 nm, and 43.3 V m^{-1} at 658 nm was respectively noticed for HGN@CdS-1, HGN@CdS-2, and HGN@CdS-3. Compared with pure CdS, the three HGN@CdS attained nearly 30-fold enhancement in total electric field at the incident wavelength of around 650 nm. This outcome demonstrated the promise of exploiting the LSPR-induced electric field amplification for facilitating additional generation of charge carries for HGN@CdS and thereby increasing the photocatalytic performance.

2.4. Photocatalytic H$_2$ Production

Photocatalytic H$_2$ production was carried out under visible light illumination ($\lambda = 400$–700 nm). In order to offer a direct activity comparison among HGN@CdS with various shell thicknesses, the particle number of each sample was kept a fixed value (3.4 × 10^{11}). The detailed procedures of controlling the particle number for each sample were addressed in the Supporting Information. As shown in **Figure 6a**, the three HGN@CdS samples showed drastic increases in H$_2$ production yield over pure CdS and pure HGN. This result verified that an increase in photocatalytic activity could be achieved by the synergetic interaction between HGN and CdS. Further activity comparison with cit-Au@CdS and HGN+CdS may highlight the superior feature of the double-hollow yolk@shell nanostructures in H$_2$ production. As revealed in Figure S10a (Supporting Information), cit-Au@CdS was inferior to HGN@CdS-2 in H$_2$ production yield, supporting that the photocatalytic efficiency could be improved by exploiting the hollow structure of the plasmonic metal yolk. On the other hand, the performance of HGN+CdS was considerably lower than that of HGN@CdS-2. According to the TEM observations from Figure S10b (Supporting Information), HGN+CdS had severe HGN aggregation. Only a small amount of HGN was in contact with CdS, which compromised the effectiveness of interfacial charge transfer and led to mediocre H$_2$ production ac-

tivity. This result further highlighted the benefits of yolk@shell nanostructures.

The H$_2$ production yield of HGN@CdS-1, HGN@CdS-2 and HGN@CdS-3 was respectively 0.71, 7.74 and 9.90 µmol h^{-1}. Apparently, the sample with the largest shell thickness exhibited the highest H$_2$ production yield. As derived from the TA analytic results, the variation of interfacial charge dynamics with CdS shell thickness did not show a consistent trend with the variation of photocatalytic performance. This outcome implied that there existed other factors influencing the photocatalytic behavior for the current HGN@CdS. Note that the particle number of the three HGN@CdS added in H$_2$ production experiments was kept identical. Under this situation, the sample with the largest CdS shell thickness was expected to have the highest CdS content and thereby harvest the most abundant photons. This would partially contribute to the highest H$_2$ production yield of HGN@CdS-3. To exclude the contribution of CdS content, the H$_2$ production yields of the three HGN@CdS were normalized to the weight of the composed CdS, giving a specific H$_2$ production yield of 0.67, 2.61 and 2.32 mmol h^{-1} g$_{CdS}$$^{-1}$ for HGN@CdS-1, HGN@CdS-2 and HGN@CdS-3, respectively. Interestingly, HGN@CdS-2 with a medium shell thickness exhibited the highest specific H$_2$ production yield. In other words, under a fixed CdS content, an optimal shell thickness can endow HGN@CdS with the most efficient H$_2$ production activity. This outcome disclosed that shell thickness was a decisive factor dictating the photocatalytic performance of HGN@CdS. Because the diffusion of H$^+$/H$_2$ across the shell was necessary for maintaining sustained H$_2$ production, the mass transport kinetics across the shell and their dependence on shell thickness should be considered. To explore the molecular diffusion behavior in HGN@CdS, rhodamine B (RhB) was used as an optical indicator for molecular release tracing. The comparative results among the three HGN@CdS were displayed in Figure S11 (Supporting Information). For quantitative comparison, the diffusion coefficient (D) of RhB across the CdS shell was estimated through curve fitting with the following equation:[61]

$$\frac{M_t}{M_\infty} = 1 - \frac{6}{\pi^2} \sum_{n=1}^{\infty} \frac{1}{n^2} \exp\left(-\frac{\pi^2 D n^2 t}{R_s^2}\right) \quad (1)$$
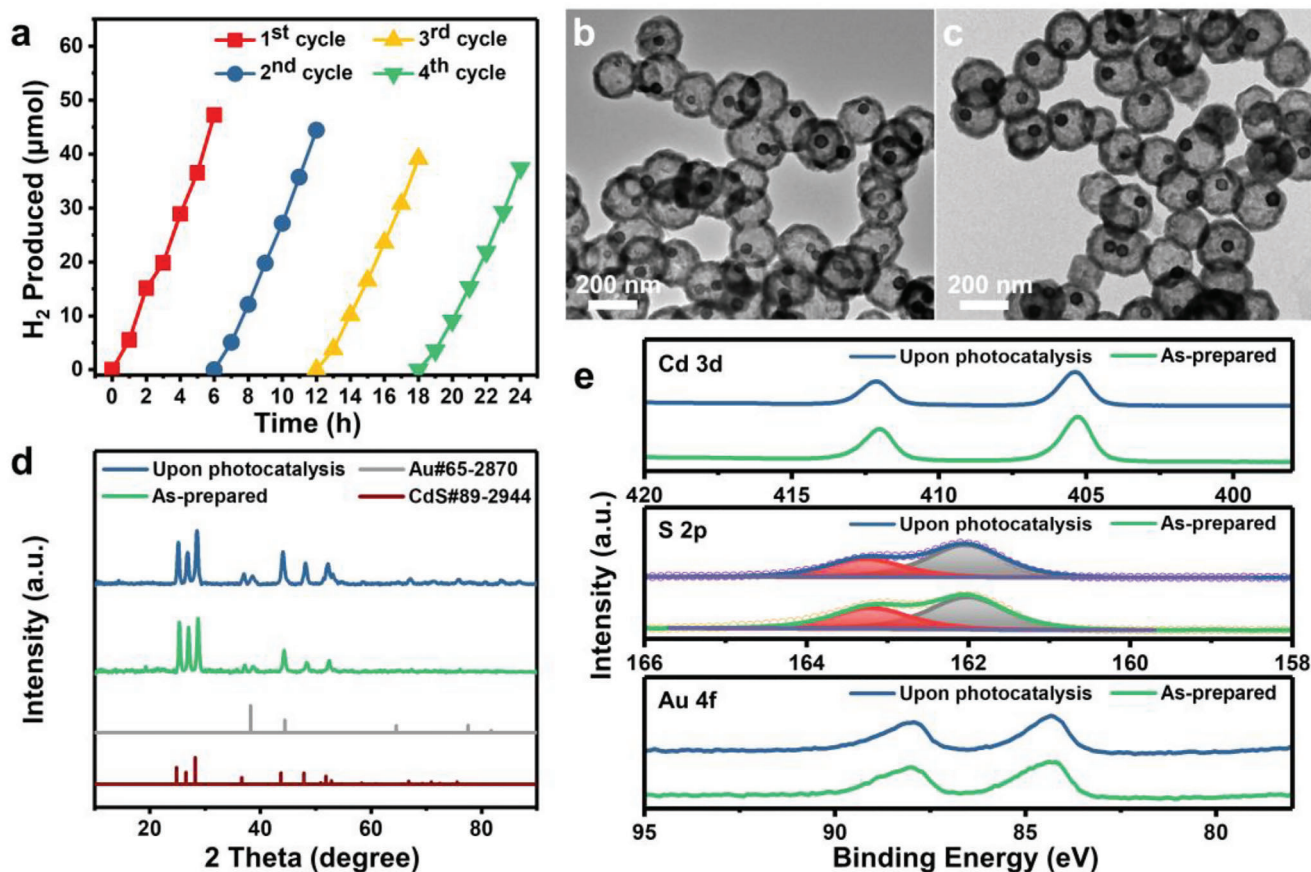
where M$_t$/M$_\infty$ is the fraction of the released RhB at time t, and R$_s$ is the radius of the CdS shell. The computed D value was 9.44

ADVANCED
SCIENCE NEWS

www.advancedsciencenews.com

ADVANCED
FUNCTIONAL
MATERIALS

www.afm-journal.de

$\times 10^{-20}$, 1.49×10^{-18}, and 1.18×10^{-18} m^2 s^{-1} for HGN@CdS-1, HGN@CdS-2, and HGN@CdS-3 respectively. Among the three HGN@CdS, HGN@CdS-2 showed the highest D value. Since the particle number of the three HGN@CdS was identical, the sample with a thicker shell should possess a larger total surface area. By using the geometrical and size distribution information, the total surface area of HGN@CdS can be calculated. The details of calculations were specified in the Supporting Information. For HGN@CdS-1, HGN@CdS-2, and HGN@CdS-3, the calculated total surface area was 6.49×10^2, 7.38×10^2 and 8.19×10^2 m^2, respectively. As the shell thickness increased, a greater extent of shell surface exposure resulted, which is beneficial for molecule transport across the shell. Nevertheless, a thicker shell can prohibit molecules from efficient diffusion due to the limited diffusion length. These two opposite factors may compete to bring forth the best molecular diffusion kinetics observed for HGN@CdS-2. According to the results of RhB releasing experiments, shell thickness associated with mass transport kinetics was considered an important factor that can be maneuvered for performance optimization of HGN@CdS.

The wavelength-dependent H$_2$ production activity of HGN@CdS-2 and pure CdS was assessed under monochromatic illumination from 320 to 810 nm, and the corresponding apparent quantum yield (AQY) was compared in Figure 6b. The AQY spectra for both samples showed similar distribution with the corresponding DRS spectra in Figure S2 (Supporting Information). Pure CdS had ordinary H$_2$ production efficiency across 300 to 540 nm region and achieved the highest efficiency of approximately 2.0% at 450 nm. Beyond 540 nm, no H$_2$ yield was observed, a classical behavior of CdS, in which most visible light could not be effectively used to drive photocatalytic reactions because of its medium bandgap. Compared to pure CdS, HGN@CdS-2 exhibited a significant enhancement in AQY from 300 to 800 nm. The AQY reached 4.8% at 450 nm, more than twice the performance of pure CdS, which was ascribed to the enhanced charge separation induced by HGN. Unlike pure CdS which was inactive beyond 540 nm, HGN@CdS-2 exhibited noticeable activities from 540 to 800 nm, attaining a peaked AQY of 2.3% at 660 nm. It should be noted that these AQY values were pristine without the aid of co-catalysts. By introducing suitable co-catalysts, the activity of HGN@CdS toward H$_2$ production can be further elevated. To demonstrate this feasibility, Rh/Rh$_2$S$_3$ co-catalysts were introduced to HGN@CdS by in situ photodeposition method.[62] As shown in Figure S12a (Supporting Information), upon Rh/Rh$_2$S$_3$ introduction, HGN@CdS-2 exhibited a drastic increment in H$_2$ production yield. A non-monotonic dependence of H$_2$ production yield on Rh/Rh$_2$S$_3$ content was observed. A maximal H$_2$ production yield of 40.7 µmol h^{-1} can be attained by introducing 20 wt.% Rh/Rh$_2$S$_3$. This yield exceeded 5 times the activity of HGN@CdS-2 without Rh/Rh$_2$S$_3$ loading. The comprehensive analysis by Raman and XPS measurements (Figure S12b–d, Supporting Information) showed that the introduced Rh/Rh$_2$S$_3$ consisted of Rh$_2$S$_3$ in majority and a trace amount of Rh. The HRTEM images and TEM-EDS mapping data in Figures S13 and S14 (Supporting Information) further revealed the chemical composition of Rh/Rh$_2$S$_3$ and its uniform deposition on the surface of HGN@CdS. As highlighted by the star marks in Figure 6b, by introducing 20 wt.% Rh/Rh$_2$S$_3$ co-catalysts, the

H$_2$ production activity of HGN@CdS across 300 to 800 nm region can be greatly enhanced, achieving an AQY of 8.2%, 6.2% and 4.4% at 320 nm, 420 nm and 660 nm, respectively. The noticeable activity from 540 to 800 nm clearly illustrated that the LSPR of HGN could practically contribute to H$_2$ production of CdS. Two possible mechanisms associated with the LSPR-enhanced activity of HGN@CdS were considered, i.e., hot electron injection and electric field magnification.[10] Upon LSPR excitation, the coherent electron oscillation of HGN could decay via Landau damping, forming highly energetic electron-hole pairs through interband transition.[63] During the relaxation processes, the hot electrons could transfer to the adjacent CdS, survive sufficiently long, and participate in H$_2$ production, which provided HGN@CdS with enhanced activities at the wavelength region where the LSPR of HGN was located. The results of TA measurements validated the contention of hot electron injection. Another possible contributing mechanism was the localized electric field magnification induced by LSPR. As illustrated in FDTD simulations, HGN functioned as a concentrator to greatly amplify the electric field for CdS. The magnified electric field can promote charge carrier generation for CdS since the formation rate of charge carriers is proportional to the square of the electric field intensity.[64] Due to the low energy of LSPR of HGN, such electric field magnification was merely utilized to promote defect-related intraband transition of CdS, bringing forth additional activities beyond the bandgap absorption. This mechanism contributed to the enhanced activities beyond 540 nm as well. To highlight the superiority of the current HGN@CdS in H$_2$ production, its performance was compared with the state-of-the-art CdS-based photocatalysts reported in the literature. As summarized in Table S2 (Supporting Information), most of the CdS-based photocatalysts can attain an AQY exceeding 5.0% at 420 nm. The highest AQY was attained by single-atom Ni-immobilized CdS,[65] which can reach as high as 27.6% at 400 nm, substantially higher than the value of the current HGN@CdS. It should be, however, pointed out that those seemingly outstanding CdS-based photocatalysts were merely responsive to the wavelength region within the bandgap transition; beyond bandgap absorption, i.e., the wavelength longer than 550 nm, they barely exhibited photocatalytic activity due to the incapability of harvesting photons. As noticed in Figure 6b, the photocatalytic activity of HGN@CdS can be extended to near infrared region thanks to the plasmonic effect of HGN. In fact, the achievable AQY of HGN@CdS under LSPR excitation (4.4% at 660 nm) was unprecedented. As Table S3 (Supporting Information) summarizes, the current HGN@CdS exhibited a record-breaking LSPR-induced AQY of 4.4% at 660 nm in comparison with the state-of-the-art Au-decorated plasmonic photocatalysts reported so far. This feature is particularly important to the realization of full spectrum-driven H$_2$ production since there are only few choices among the currently available photocatalysts that can respond to near infrared irradiation.

The long-term stability of photocatalysts is also a pivotal factor for realistic applications. To examine the stability, the samples were repeatedly used and recycled in H$_2$ production reactions. In **Figure 7a**, the H$_2$ production of HGN@CdS-2 in four consecutive cycles of operations was monitored. A gradual decrease in H$_2$ production yield was observed, from 7.87 µmol h^{-1} at the 1st cycle to 6.23 µmol h^{-1} at the 4th cycle. On account of the electrolyte

ADVANCED
SCIENCE NEWS
www.advancedsciencenews.com

ADVANCED
FUNCTIONAL
MATERIALS
www.afm-journal.de

Figure 7. a) Results of stability tests on HGN@CdS-2 for photocatalytic H_2 production. Corresponding TEM images of HGN@CdS-2, b) before and c) after photocatalysis. d) XRD patterns, e) XPS spectra of HGN@CdS-2 before and after photocatalysis.

refreshment and sample collection between each cycle, the loss of photocatalyst powder was inevitable, which was believed to be the main cause for the observed activity loss. To validate this proposition, the microstructure, crystallographic structure and chemical states of the used HGN@CdS-2 were further examined. The TEM images shown in Figure 7b,c revealed that the yolk@shell nanostructures remained intact after repeatedly used. The XRD patterns in Figure 7d showed that the crystal structure of the used HGN@CdS was nearly unchanged. The corresponding XPS spectra in Figure 7e also disclosed the high integrity of chemical states for the used HGN@CdS. The recorded binding energies of Au 4f, Cd 3d and S 2p complied with the values reported for Au[66] and CdS.[67] The spectral features were also in accordance with those obtained in the as-prepared HGN@CdS. Significantly, signal of sulfur element located at 164.4 eV associated with the photocorrosion of CdS was not observed,[68,69] which accounted for the high stability of HGN@CdS toward photocatalytic H_2 production.

2.5. Photoelectrochemical Properties

Photoelectrochemical (PEC) measurements were conducted on relevant samples under visible light illumination ($\lambda = 400$–700 nm) to evaluate their applicability in PEC reactions. The anal-

yses included linear-sweep voltammetry (I–V curves), chronoamperometry (I–t curves), and electrochemical impedance spectroscopy (Nyquist plots), with results presented in Figure S15 (Supporting Information). The data revealed several noteworthy findings. First, the three HGN@CdS electrodes, compared to pure CdS, demonstrated superior PEC performance characterized by higher photocurrent densities and reduced onset potentials. Specifically, photocurrent densities at +0.45 V versus RHE were recorded as 15.0, 17.2, 38.6, and 60.3 $\mu A\ cm^{-2}$ for pure CdS, HGN@CdS-1, HGN@CdS-2, and HGN@CdS-3, respectively, with corresponding onset potentials of 0.19, 0.03, −0.14, and −0.16 V versus RHE. This enhancement in PEC activity was attributed to the synergistic effects between HGN and CdS. Second, of the three, HGN@CdS-3 exhibited the most pronounced improvement in PEC performance, aligning with the photocatalytic H_2 production results shown in Figure 6a. Third, pure HGN alone showed minimal response toward visible light, reflecting its inherently low PEC efficiency, a finding corroborated by its negligible photocatalytic H_2 production capability. Nyquist plot analysis, on the other hand, revealed that the three HGN@CdS electrodes possessed a compressed arc compared to pure CdS, suggesting improved charge transfer resistance for HGN@CdS. The fitted data in Table S4 (Supporting Information) further supported this suggestion by showing reduced bulk (R_1) and interfacial (R_2) charge transfer resistances for HGN@CdS
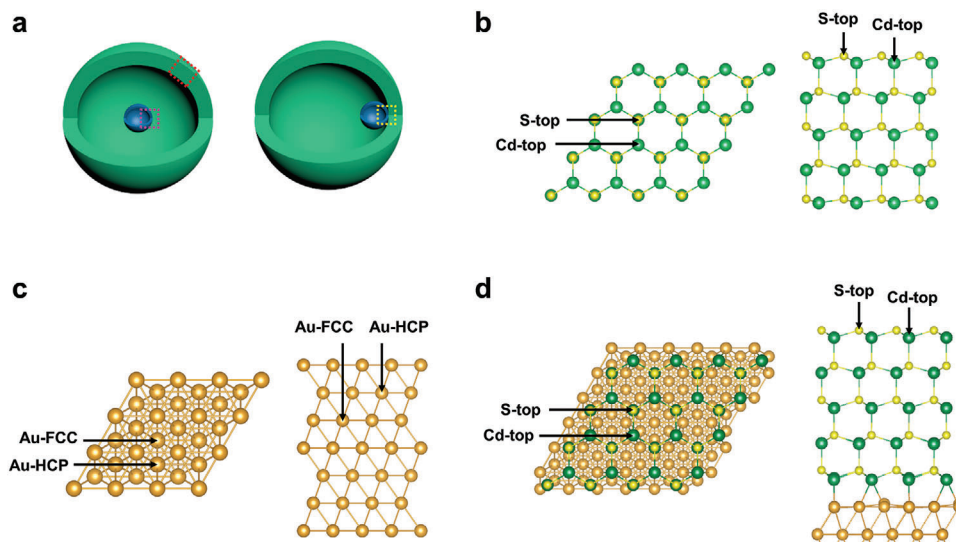
Figure 8. a) Schematic illustration of simulated models for HGN@CdS and b–d) the corresponding top view and side view of the constructed supercells for DFT calculations. The gold, green, and yellow spheres represented the Au, Cd, and S atoms, respectively. The black arrows in b-d) pointed to the possible hydrogen adsorption sites.
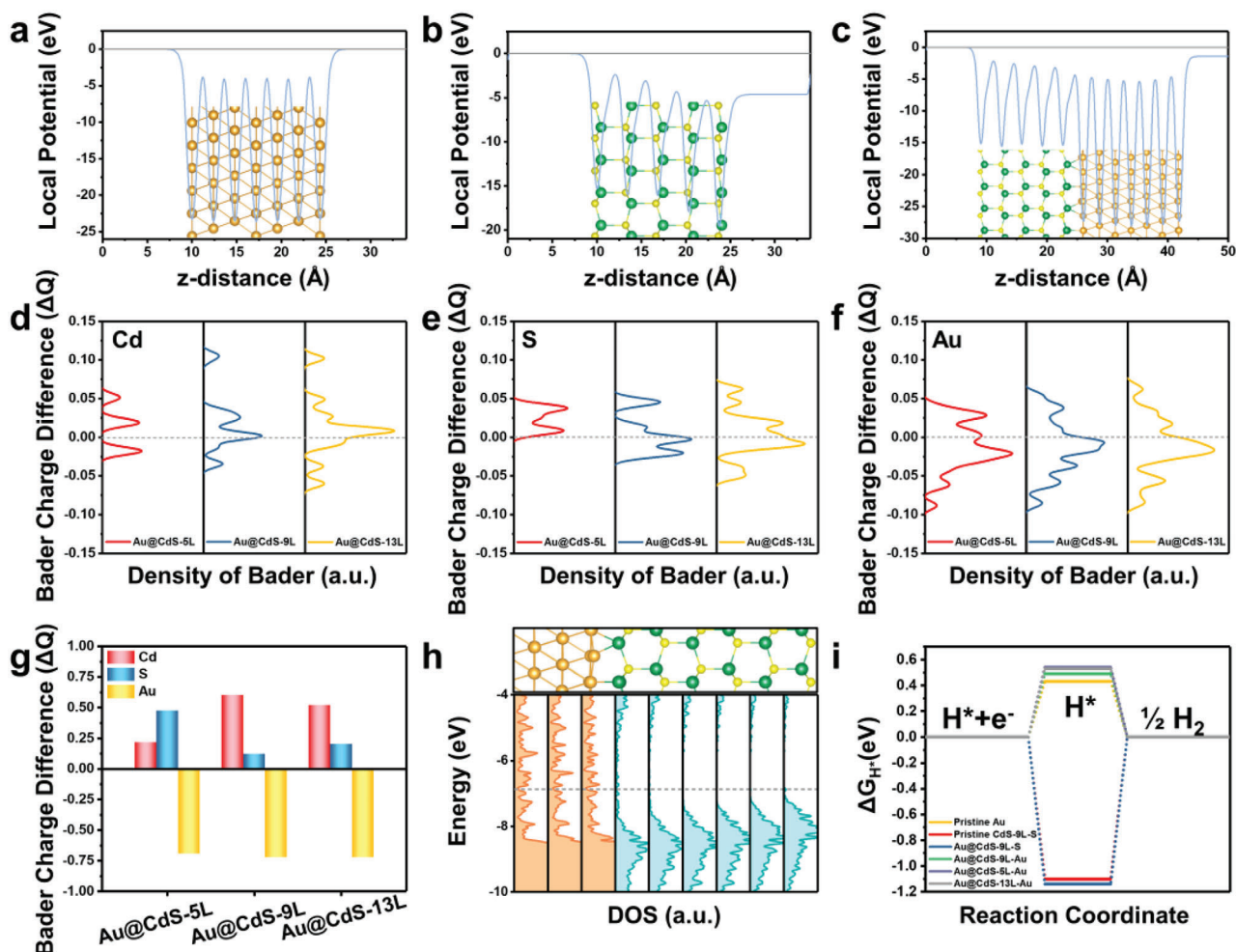
electrodes. The computed R_1 and R_2 values were 6.1 and 16.7 kΩ for pure CdS, 5.9 and 10.1 kΩ for HGN@CdS-1, 1.3 and 2.8 kΩ for HGN@CdS-2, and 1.2 and 2.1 kΩ for HGN@CdS-3. Note that pure HGN showed considerably low charge transfer resistance (R_1 = 2.5 kΩ, R_2 = 8.3 kΩ). Despite this feature, the minimal photoresponse of pure HGN constrained its applicability in PEC reactions. The consistency between Nyquist plot outcomes and PEC data underscores that the improved charge transfer resistance facilitated by HGN contributed to the elevated PEC activity of HGN@CdS.

2.6. DFT Simulations and Photocatalytic Mechanism

Further insights into how photocatalytic reactions occurred over HGN@CdS at a molecular level were gained by conducting density functional theory (DFT) calculations. **Figure** 8a illustrates two simulation models for HGN@CdS. In the first model, the HGN yolk was positioned at the center of the void space, isolated from the CdS shell. This configuration can be considered as the separate existence of pristine Au surface (indicated by purple dashed square) and pristine CdS surface (indicated by red dashed square). The corresponding supercells are depicted in Figure 8b,c. In the second mode, the HGN core was in direct contact with the CdS shell. The HGN/CdS heterojunction (indicated by yellow dashed square) was modeled by stacking the slab of CdS(0001) on that of Au(111). The constructed supercells, denoted as Au@CdS, are displayed in Figure 8d. Note that the slab number of CdS(0001) was varied from 5 layers (CdS-5L), 9 layers (CdS-9L) to 13 layers (CdS-13L) in order to simulate the conditions of various shell thicknesses for HGN@CdS.

Figure 9a–c present the electrostatic potential distribution along the surface normal direction for pristine Au surface, pristine CdS-5L surface, and Au@CdS-5L surface. Here, the two pristine surfaces represented a scenario, where HGN and CdS were met before contact. The Au@CdS-5L surface, on the other hand,

reflected a situation, in which HGN and CdS were brought into contact. In both pre- and post-contact conditions, the average local potential of the Au surface was lower than that of the CdS surface, suggesting a tendency of electron transfer from CdS to Au. Consistent electrostatic potential characteristics remained evident when increasing the slab number of CdS, which can be identified from the computed data on Au@CdS-9L and Au@CdS-13L in Figure S16 (Supporting Information). To further evaluate the charge transfer behavior, we performed Bader charge difference analysis on each atom for the three Au@CdS models. The computed charge differences of individual atoms are shown in Figure S17 (Supporting Information). Figure 9d–f present the summarized profiles of density of Bader (DOB). Here, DOB was used to describe the statistical distribution of charge differences for total atoms by using Gaussian function. For Cd atoms, the strongest DOB peak shifted toward positive side as the slab number of CdS increased, implying that more Cd atoms lost electrons for larger CdS slabs. Conversely, the DOB profiles of S atoms shifted negatively, showing a reduced extent in electron transfer to Au. For Au atoms, the highest DOB peak was negative and showed a negligible change with the slab number of CdS, indicating that Au tended to receive electrons regardless of the change of the slab number of CdS. The total Bader charge difference of each atom is further summarized in Figure 9g and Table S5 (Supporting Information). For Au@CdS-13L, the total Bader charge difference of Cd, S, and Au atoms was 0.519, 0.204, and −0.723 e, respectively. Combining these features with the DOB data, it can be concluded that electrons would transfer from CdS to Au and this event did not show direct correlation with the slab number of CdS. The simulation results from electrostatic potential and Bader charge difference analysis strongly complied with the experimental observations. Figure 9h illustrates the layer-projected density of states (DOS) for Au@CdS-9L and the corresponding atomic structure. The DOS distribution of CdS (highlighted by cyan) shifted toward lower energy as it approached the Au/CdS interface. This finding was consistent with the electrostatic

ADVANCED
SCIENCE NEWS
www.advancedsciencenews.com

ADVANCED
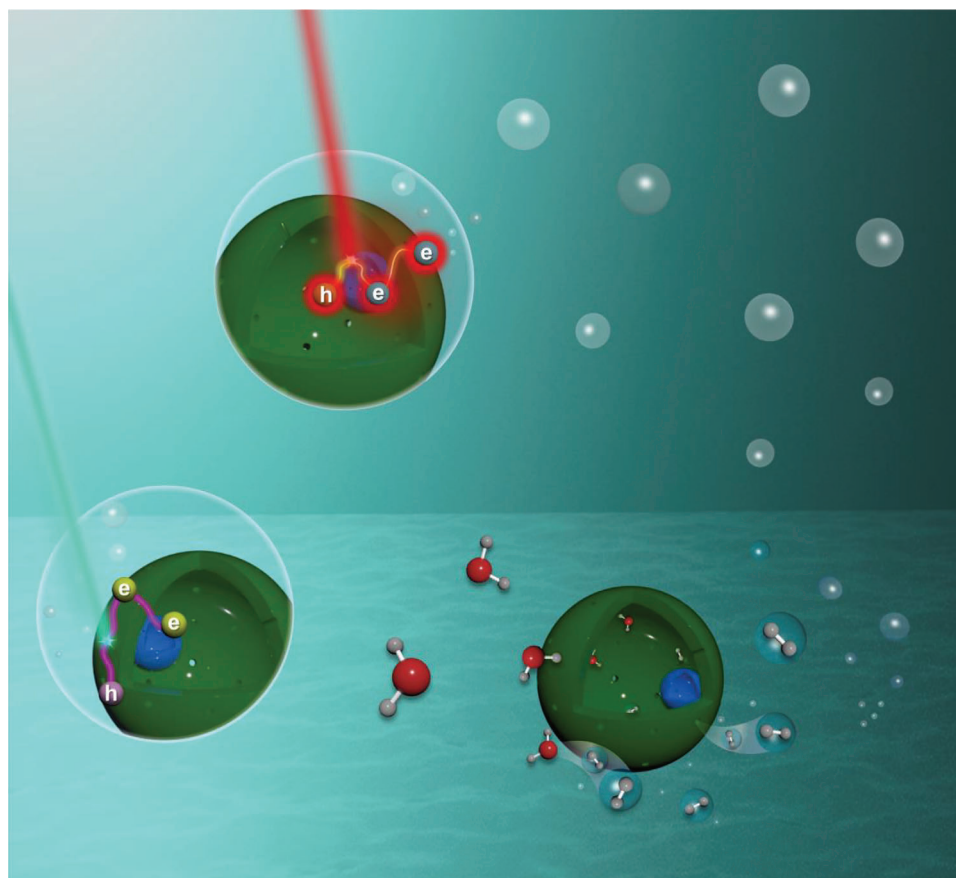**FUNCTIONAL**
MATERIALS
www.afm-journal.de

Figure 9. Electrostatic potential distribution along the surface normal of the slabs for a) Au(111), b) CdS-5L, and c) Au@CdS-5L. The vacuum level was set to 0 eV. d–f) Bader charge difference of Cd, S and Au atoms, g) Bader charge difference of total atoms for the three Au@CdS models. h) Layer-projected DOS profiles and the corresponding atomic structure for Au@CdS-9L. Each CdS layer was composed of one Cd atomic layer and one S atomic layer. The vacuum level was aligned to 0 eV, and the Fermi level was labeled by a gray dashed line. i) Computed ΔG_{H*} values at various surficial sites, including Au-fcc site of pristine Au, S-top site of pristine CdS-9L, S-top site of Au@CdS-9L, Au-hcp site of Au@CdS-9L, Au-fcc site of Au@CdS-5L, and Au-hcp site of Au@CdS-13L.

potential results, in which preferable electron transfer from CdS to Au was considered. Noticeably, additional energy states were observed in the bandgap of CdS, presumably resulting from the electronic hybridization of CdS and Au states at the interface. Due to the wavefunction overlap of energy states between CdS and Au, charge transfer from CdS to Au may be further promoted under light illumination.

The Gibbs free energy of hydrogen adsorption (ΔG_{H*}) on various surficial sites of Au@CdS models was further calculated to evaluate the intrinsic catalytic activity toward H_2 evolution reaction. The calculations on pristine Au and pristine CdS were also performed to obtain a comparative result. According to the Sabatier principle, ideal catalysts for H_2 evolution should have a $|\Delta G_{H*}|$ value close to zero.[70] Due to the significantly high ΔG_{H*} values calculated for the Cd sites in both Au@CdS and pristine CdS, additional analysis focused on the results pertaining to the Au and S sites was conducted. As shown in Figure 9i and Table S6 (Supporting Information), the computed ΔG_{H*}

values for Au@CdS-5L (Au-fcc site), Au@CdS-9L (Au-hcp site), Au@CdS-13L (Au-hcp site), and Au@CdS-9L (S-top site) were 0.54, 0.49, 0.53, and −1.14 eV, respectively. Apparently, Au sites were more thermodynamically favorable than S sites for catalyzing H_2 evolution over Au@CdS. This outcome indicated that Au could be the primary active sites for conducting solar H_2 production on the current HGN@CdS. Compared to pristine CdS ($\Delta G_{H*} = -1.10$ eV for CdS-9L (S-top)), the relatively small $|\Delta G_{H*}|$ values of the three Au@CdS models with Au sites demonstrated that H_2 evolution on the Au sites of Au@CdS was more effective than the S sites on pristine CdS. This finding supported the experimental observations on the superiority of HGN@CdS to pure CdS in photocatalytic H_2 production. On the other hand, while pristine Au also owned an appropriate ΔG_{H*} value (0.43 eV), its naturally low photocatalytic efficiency limited the potential for solar H_2 production. Based on the theoretical predictions and experimental observations, a plausible mechanism was proposed to understand the enhanced photocatalytic performance of

**ADVANCED
SCIENCE NEWS**

www.advancedsciencenews.com

**ADVANCED
FUNCTIONAL
MATERIALS**

www.afm-journal.de

Figure 10. Proposed mechanism of photocatalytic H_2 production on HGN@CdS under band edge excitation and plasmonic excitation.

HGN@CdS. As illustrated in **Figure 10**, under band edge excitation (as represented by a green beam), the photoexcited electrons and holes were produced in CdS. Owing to the downward band bending at interface, the photoexcited electrons of CdS were favorably transported to HGN. As derived from DFT calculations, the surface of HGN may function as primary active sites for H_2 evolution. The delocalized electrons at HGN can readily reduce protons to evolve H_2. As derived from the TA data, the creation of charge separation state at the HGN/CdS heterojunction can guarantee the separated electrons again charge recombination, which accounted for the substantially enhanced H_2 production activity for HGN@CdS. Under plasmonic excitation (as marked by a red beam), the hot electrons generated at HGN can be injected into CdS. As the TA analysis shows, the delocalized hot electrons were considerably long-lived with a lifetime up to 337 ps (for HGN@CdS-3), achieving noticeable H_2 production activity as observed. Furthermore, the magnified electric field induced by the LSPR of HGN promoted additional charge carrier generation for CdS, contributing to the enhanced photocatalytic activities as well. By adjusting the shell thickness, the mass transport kinetics can be coordinated to achieve performance optimization for HGN@CdS.

To elucidate the charge transfer mechanism within HGN@CdS, we performed selectively photodeposition experiments under two wavelength ranges. First, we utilized photodeposition of PbO_2 to investigate the charge transfer path-

way of HGN@CdS under band edge excitation. When subjected to irradiation at $\lambda = 400–550$ nm, the photoexcited electrons in CdS were transferred to the HGN, resulting in the accumulation of photogenerated holes within the CdS. These localized holes facilitated the oxidation of Pb^{2+} ions present in the solution,[71] leading to the selective deposition of PbO_2 on the CdS surface. This was evidenced by the detection of PbO_2 lattice fringes adjacent to CdS, as well as the uniform distribution of Pb signals throughout the CdS shell region, as illustrated in Figure S18 (Supporting Information). These observations corroborate the hypothesized electron-hole separation mechanism under band edge excitation. Furthermore, to delineate the charge transfer process under plasmonic excitation, photodeposition of Pt was explored. With irradiation at $\lambda > 550$ nm, the hot electrons generated within HGN were transferred to CdS, facilitating the reduction of Pt^{4+} ions[72] and subsequent deposition of Pt on the CdS surface. The selective localization of Pt on the CdS, as demonstrated in Figure S19 (Supporting Information), validates the proposed hot electron injection mechanism under plasmonic excitation.

2.7. Cost Analysis and Practical Applicability

To evaluate the industrial applicability of HGN@CdS, a cost analysis based on supplier catalog prices was performed, alongside

**ADVANCED
SCIENCE NEWS**

www.advancedsciencenews.com

**ADVANCED
FUNCTIONAL
MATERIALS**

www.afm-journal.de

a practical demonstration of their use in real-world scenarios. This multifaceted approach encompasses both the economic and functional aspects necessary for industrial-scale production and application. A cost analysis for the synthesis of HGN@CdS was performed based on the prices listed on supplier websites. As presented in Table S7 (Supporting Information), the total estimated cost for producing 1 g of HGN@CdS-2 was $197.5. To enhance cost efficiency in large-scale production, strategies such as bulk purchasing of raw materials, recycling solvents, and refining synthesis methods will be explored. Additionally, the practical applicability of HGN@CdS in real-world scenarios has been demonstrated through the use of the produced H_2 to power an electric device. This was achieved by employing a given quantity of HGN@CdS-2, loaded with 20 wt.% Rh/Rh_2S_3 as photocatalysts for H_2 production. As evidenced in Video S1 (Supporting Information), the H_2 accumulated over 40 h of visible light irradiation was utilized to operate a customized H_2 fuel cell, resulting in a total power output of 16.4 mW. This enabled the continuous operation of an electric mini fan for 17 s, highlighting the potential of HGN@CdS as an effective photocatalyst for H_2 production and its subsequent application in powering electric devices.

3. Conclusions

In conclusion, we have demonstrated the use of HGN@CdS as superior plasmonic photocatalysts for practical solar H_2 production. The AQY of H_2 production can reach 8.2% at 320 nm, 6.2% at 420 nm, and 4.4% at 660 nm. The plasmon-enhanced activity at 660 nm is exceptional, surpassing the state-of-the-art Au-decorated plasmonic photocatalysts reported so far. The superiority of HGN@CdS originates from the creation of charge separation state at HGN/CdS heterojunction, the considerably long-lived hot electrons of plasmonic HGN, the magnified electric field, and the advantageous features of double-hollow yolk@shell nanostructures. The current study not only delivers a new type of plasmonic photocatalyst paradigms enabling efficient H_2 production from the untapped near infrared energy, but also illustrates the utility of the novel HGN nanostructures in plasmonic photocatalysis. The finding of this work offers a promising strategy to the expansion of the photoresponse range for the currently available photocatalysts in order to realize full-spectrum driven solar H_2 production.

4. Experimental Section

Synthesis of HGN: HGN was synthesized by conducting galvanic replacement on sacrificial templates in an anaerobic environment.[73] First, a mixture of 1.0 mL trisodium citrate dihydrate ($Na_3C_6H_5O_7 \cdot 2H_2O$, 0.4 M), 100 µL cobalt(II) chloride ($CoCl_2$, 0.4 M) and 98.9 mL deionized (DI) water were mixed in the flask under argon purge for 1 h. With an injection of 0.4 mL of sodium borohydride ($NaBH_4$ 1.0 M), the solution turned brown, indicating the formation of Co_xB_y scaffolds. After 2 min of stirring, the solution was kept steady without disturbing to enable Co_xB_y aging and $NaBH_4$ hydrolysis for another hour. At the same time, another solution containing 80 µL tetrachloroauric(III) acid ($HAuCl_4$, 0.01 M) and 15 mL DI water was mixed in a flask under nitrogen flow for 1 h. Next, 15 mL of Co_xB_y was transferred into the above solution using a cannula to avoid oxygen exposure. Based on the reduction potential difference (Co^{2+}/Co, $E_0 = -0.277$ V versus SHE;[39] $AuCl_4^-/Au$, $E_0 = 0.994$ V versus SHE),[40] the Au^{3+} ion was reduced on the surface of Co_xB_y and formed Co_xB_y@Au

core@shell nanoparticles. After stirring for 2 min, the entire system was exposed to air to allow oxidative etching upon Co_xB_y. The resulting HGN was collected by centrifugation at 12 000 rpm twice to remove residual ions.

Solid cit-Au nanoparticles were synthesized by a typical citrate reduction method. Briefly, 2.5 mL $HAuCl_4$ (0.01 M) was added to 97.5 mL boiling DI water, then 70 µL $Na_3C_6H_5O_7 \cdot 2H_2O$ (0.5 M) was injected, and the solution was boiled for 10 min. After the color changed from transparent to black and then became fuchsia, the entire system was cooled down and directly used for further synthesis without washing.

Synthesis of HGN@CdS: HGN@CdS was derived from the HGN@Cu_2O core@shell nanostructure template. To synthesize HGN@Cu_2O, 3.0 mL of HGN was dispersed in 46 mL of DI water and 4.0 mL of copper sulfate ($CuSO_4$, 0.01 M) aqueous solution. Subsequently, 4.0 mL of sodium hydroxide (NaOH, 1.0 M) and 2.0 mL of L-ascorbic acid (0.1 M) were simultaneously added into the above solution. After aging for 10 min, the color of the mixed solution changed, indicating the formation of HGN@Cu_2O. Afterward, sodium sulfide (Na_2S, 0.1 M) was introduced to the HGN@Cu_2O suspension. Because of the nanoscale Kirkendall effect, the solid Cu_2O shell was transformed into a hollow Cu_7S_4 shell,[26] causing the formation of HGN@Cu_7S_4 yolk@shell nanostructures. The precipitate was centrifuged and subjected to acidic washing with 0.1 M hydrogen chloride (HCl) to remove the remaining Cu_2O. To prepare for HGN@CdS, the HGN@Cu_7S_4 powder was redispersed in 10 mL methanol in a water bath at 55 °C. Subsequently, 178 µL trioctylphosphine (0.4 M in toluene) and 4.0 mL of cadmium nitrate ($Cd(NO_3)_2$, 0.2 M in methanol) were added dropwise in order. The cation exchange reaction was allowed to proceed for 6 h. The color of the solution gradually turned green, signifying the substitution of Cu by Cd. The product was collected by centrifugation and washed with methanol three times. To adjust the shell thickness, 70 µL, 320 µL and 2.4 mL of Na_2S were separately added during the synthesis of HGN@Cu_7S_4. The shell thickness of the resulting HGN@CdS was modified accordingly to 7.7 ± 1.8, 18.4 ± 2.9 and 24.5 ± 3.3 nm. These samples were denoted as HGN@CdS-1, HGN@CdS-2 and HGN@CdS-3, respectively. For comparison purposes, cit-Au@CdS yolk@shell nanostructures, pure hollow CdS and a physical mixture of pure HGN and pure CdS (HGN+CdS) were also prepared. Here, cit-Au@CdS was synthesized by using cit-Au as the core for deposition of Cu_2O, followed by the same ion exchange reaction processes described above. Pure hollow CdS was synthesized by conducting the same ion exchange reaction processes on pure Cu_2O. Moreover, HGN+CdS was obtained by simply mixing pure HGN and pure CdS suspension with the composed HGN to CdS ratio deliberately adjusted to equate that of HGN@CdS-2.

Characterizations: TEM images were taken on a JEOL JEM-F200 microscope. High-resolution TEM images, EDS mapping, and SAED patterns were acquired from JEOL JEM-ARM200FTH. XRD patterns were obtained with a Bruker D2 PHASER diffractometer. UV–vis absorption spectroscopy and DRS were performed using Hitachi U-3900H and JASCO V-670 spectrophotometers, respectively. To obtain steady–state PL spectra, a Hitachi F-4500 fluorescence spectrometer was used. XPS and UPS data were collected from Thermo Fisher Scientific ESCALAB Xi+ with an Al anode and He I (21.22 eV) as the irradiation source, respectively. Raman spectroscopy measurements were carried out on a micro-Raman spectrometer (MRID, Protrustech, Taiwan) with a diode-pumped solid-state laser of Nd:YAG ($\lambda = 532$ nm). For photo-KPFM measurements, surface potential was recorded on a Nanoscope III spectrometer (Digital Instruments) in the dark and under UV-B illumination ($\lambda = 312$ nm, 4 W) at room temperature. The chemical composition of HGN@CdS was quantitatively analyzed using ICP-MS (Thermo Fisher Scientific, iCAP TQ).

Photocatalytic H_2 Production: The photocatalytic H_2 production reaction was carried out in a customized quartz reactor. Seven relevant samples, including the three HGN@CdS, cit-Au@CdS, pure CdS, pure HGN and CdS+HGN, were tested and compared. Note that in order to offer a direct activity comparison among HGN@CdS with various shell thicknesses, the particle number of each samples except HGN+CdS was kept a fixed value. To have a fixed particle number (3.4×10^{11}), different amounts of the sample powders were employed to carry out H_2

production experiments. The detailed calculations of determining the particle number were specified in the Supporting Information. The added amount of HGN@CdS-1, HGN@CdS-2, HGN@CdS-3, cit-Au@CdS, pure CdS and pure HGN was respectively 1.3, 3.2, 4.5, 3.2, 3.3, and 0.3 mg. For HGN+CdS, the composed HGN to CdS ratio was deliberately adjusted to equate that of HGN@CdS-2. The added amount of HGN+CdS was 3.3 mg pure CdS and 0.3 mg HGN, identical to that of HGN@CdS-2. The sample powders were dispersed in 27.0 mL of 0.25 M sodium sulfide (Na_2S)/0.35 M sodium sulfite (Na_2SO_3) electrolyte. Prior to illumination, the reactor was well sealed with a septum and deaerated with argon for 30 min. The light source used for photocatalytic H_2 production was a solar simulator (Newport, LCS-100, 94 011 A) coupled with a 400–700 nm bandpass filter, generating visible light irradiation with a controlled power of 90 mW cm^{-2}. The gas product was collected every hour and analyzed with gas chromatography (Bruker, SCION 436 GC) equipped with a thermal conductivity detector. For wavelength-dependent H_2 production activity, the irradiation source was a 150 W xenon lamp combined with a monochromator (Horiba) with a 1200 gr mm^{-1} grating. The intensity of monochromatic light was measured with an optical power meter (Newport 918-D-UV-OD3R). The AQY of H_2 production was calculated using the following equation:[74]

$$AQY\ (\%) = \frac{\text{number of reacted electrons}}{\text{number of incident photons}} \times 100\%$$

$$= \frac{2 \times \text{number of } H_2 \text{ molcules}}{\text{number of incident photons}} \times 100\% \tag{2}$$

To introduce Rh/Rh_2S_3 co-catalysts, a given amount of rhodium(III) chloride ($RhCl_3$) aqueous solution (1 mg mL^{-1}) was added into the electrolyte containing photocatalyst powder. The mixed solution was then irradiated to simultaneously perform photodeposition of Rh/Rh_2S_3 and H_2 production.[62] By adjusting the volume of $RhCl_3$ added (0.16, 0.32, 0.64 to 0.96 mL), the content of the deposited Rh/Rh_2S_3 can be controlled accordingly (5, 10, 20, and 30 wt.%). For comparison purpose, pure Rh/Rh_2S_3 was also synthesized by adding 0.64 mL of $RhCl_3$ aqueous solution (1 mg mL^{-1}) into the electrolyte in the absence of photocatalyst powder. The mixed solution was then subjected to the same irradiation treatment.

Electric Field Simulation: FDTD simulations were used to compute the electric field distribution for pure HGN, pure CdS and HGN@CdS. Two representative cases of HGN@CdS were considered: i) HGN was located at the center spot of the CdS shell; ii) HGN was attached on the side spot of the CdS shell. The incident polarized light was parallel to the x-axis, and the electric field was observed along the z-axis at the central wavelength of the LSPR of HGN. The geometric parameters used for modeling were determined according to the results of the microstructural investigations. The dielectric medium surrounding the modeled structure was water (n = 1.33).

Diffusion Coefficient Estimation: RhB was used as a probe to monitor the molecular diffusion kinetics across the CdS shell of HGN@CdS. A given amount of the sample powder was dispersed in RhB solution (5.0 mL, 7.5×10^{-5} M) for 24 h to enable the complete adsorption of RhB on the sample surface. The suspension was collected by centrifugation to remove the nonadsorbed RhB. Afterward, the collected precipitate was redispersed in deionized water to release RhB. The concentration of released RhB was determined by measuring the absorption spectrum of the supernatant. The release rate of RhB was estimated by monitoring the time-dependent evolution of the absorbance of RhB at 554 nm.

XAS: XAS spectra of Cd K-edge and Au L$_3$-edge were measured at the Taiwan Photon Source beamline 44A and Taiwan Light Source beamline 13B end-stations using the total fluorescence yield (TFY) mode. Experiments were conducted under darkness and irradiation conditions. The irradiation source was a triple-A solar simulator installed with a AM 1.5 G filter (HAL-320, Asahi Spectra). Two additional filters were employed to enable band edge excitation of CdS (λ = 400–550 nm) and plasmonic excitation of HGN (λ > 550 nm). The irradiation power was 100 mW cm^{-2}

for AM 1.5 G irradiation, 22 mW cm^{-2} for irradiation at λ = 400–550 nm, and 82 mW cm^{-2} for irradiation at λ > 550 nm.

TA Spectroscopy: TA measurements were carried out in a customized spectroscopic system with a femtosecond time resolution. HGN@CdS powder was fixed on a CaF$_2$ plate with a density of 2 mg cm^{-1} and placed in a stainless steel infrared cell. Measurements were performed in 20 Torr of N_2 using a pump−probe method based in a femtosecond Ti:sapphire laser system (Spectra-Physics, Solstice & TOPAS prime; duration 90 fs; repetition rate 1 kHz). The pump pulses (370, 560, or 650 nm) with a pulse intensity of 2 μJ were introduced to excite the samples. The probe pulses were used to collect the absorption signals from 450–1000 nm. The photon signals in the visible and NIR regions were detected by a photomultiplier and InGaAs detectors.

Selective Photodeposition of PbO$_2$ and Pt: The photodeposition of PbO_2 was conducted by mixing 2.0 mg of HGN@CdS-2 and 300 μL of lead nitrate ($Pb(NO_3)_2$, 0.01 M in DI water) in 20 mL of DI water. This mixture was exposed to light irradiation at λ = 400–550 nm (22 mW cm^{-2}) for 2 h. For the photodeposition of Pt, a different solution was prepared containing 2.0 mg of HGN@CdS-2, 0.2 mL of hexachloroplatinic acid (H_2PtCl_6, 2.4 mM in methanol), and 20 mL of methanol (20 vol%). This solution was then irradiated with light at λ > 550 nm (82 mW cm^{-2}) for 2 h.

PEC Measurements: PEC measurements were performed using a three-electrode setup, which included a Pt wire as the counter electrode, Ag/AgCl (3 M KCl) as the reference electrode, and an electrolyte solution comprising 0.25 M Na_2S and 0.35 M Na_2SO_3 at pH 12.5. For the fabrication of working electrode, 1.0 mg of the sample powder was drop-cast onto a fluorine-doped tin oxide (FTO) substrate. Ni wires were then attached to the FTO using conductive silver paste. The areas of the FTO not covered by the sample were meticulously sealed with epoxy resin to prevent exposure. The PEC behavior was characterized by recording linear-sweep I–V curves at a scan rate of 0.02 mV s^{-1} and chronoamperometry I–t curves using a potentiostat (Autolab, PGSTAT204). The light source used for PEC measurements was a solar simulator (Newport, LCS-100, 94 011 A) coupled with a 400–700 nm bandpass filter, generating visible light irradiation with a controlled power of 90 mW cm^{-2}. The Nyquist plots were measured by applying alternating current signal (10 mV) over the frequency range (100 kHz to 0.001 Hz) at open circuit potential under visible light illumination.

DFT Simulation: The first-principles calculations based on DFT were performed by the Vienna ab initio simulation package (VASP).[75,76] The projected augmented wave (PAW)[77] pseudopotential approach combined with Perdew–Burke–Ernzerhof (PBE)[78] exchange-correlation function within the generalized gradient approximation (GGA)[79] was employed to calculate structure relaxation and electronic structure. The cutoff kinetic energy for the plane-wave basis set was set to 420 eV. The Brillouin-zone integration was carried out with $18 \times 18 \times 18$ and $8 \times 8 \times 6$ -centered k-point samplings for the Au and wurtzite CdS supercells, respectively. All geometric structures were relaxed until the electronic energy reached a threshold smaller than 1.0×10^{-6} eV. The optimized lattice constant of Au crystal was determined as 4.15 Å, and the optimized lattice parameters of CdS crystal were found to be a = 4.20 Å and c = 6.81 Å. The Au(111) surface was modeled using a 3×3 supercell containing 7 atomic layers. To mimic the CdS shell with varying thicknesses, the CdS surface was constructed with a (0001) stacking by a 2×2 supercell. Three models were created, incorporating 5, 9, and 13 slabs of CdS, respectively, to explore the effect of shell thickness. Au@CdS model was created by combining Au(111) surface with each of the three CdS models. To avoid the artificial interactions between periodic images along the surface normal direction, all surface models included a vacuum space exceeding 18 Å in thickness. To quantitatively evaluate the charge distribution around the atom, a grid-based Bader charge population was performed, as developed by Henkelman et al.[80,81] The Bader charge difference for each atom was defined as the difference between the Bader charge of the whole system (comprising the Au and CdS surfaces) before and after contact. A negative value for Bader charge difference means that the target atom obtains more electrons, and vice versa. The Gaussian function was employed to fit the Bader charge difference population of each atom in the Au@CdS models, which was defined as density of Bader (DOB).

The adsorption energy (E_{ads}) of H* was defined as follows:

$$E_{ads} = E_{sys} - E* - E_{surf} \qquad (3)$$

where the E_{sys} and E_{surf} were the total energies of the slab model after and before the surface adsorption, and $E*$ is the chemical potential of the adsorbate. The chemical potential of a single H atom was obtained from the energy of H_2 molecule divided by 2. The hydrogen evolution activity was evaluated using the Gibbs free energy of hydrogen adsorption, ΔG_{H*}, defined by the following equation:[82,83]

$$\Delta G_{H*} = E_{ads} + \Delta E_{ZPE} - T\Delta S_{H*} \qquad (4)$$

where ΔE_{ZPE} and ΔS_{H*} are the differences in zero-point energy and vibrational entropy between an adsorbed hydrogen and the gas phase. The calculated E_{ads} and ΔE_{ZPE} corresponding to different models and adsorption sites were provided in Table S6 (Supporting Information). The vibrational entropy of the H adsorbed system was assumed to be small,[70] so the entropy change can be evaluated as $\Delta S_{H*} = -0.5\, S^0_{H2}$, where S^0_{H2} is the entropy of hydrogen molecule in the gas phase at the standard conditions ($S^0_{H2} = 130.68$ J mol^{-1} K^{-1} at 300 K and 1 bar).[84] Therefore, the ΔG_{H*} could be treated as:

$$\Delta G_{H*} = E_{ads} + \Delta E_{ZPE} + 0.20 \qquad (5)$$

Supporting Information

Supporting Information is available from the Wiley Online Library or from the author.

Conflict of Interest

The authors declare no conflict of interest.

Data Availability Statement

The data that support the findings of this study are available from the corresponding author upon reasonable request.

[1] A. Wang, Z. Zheng, H. Wang, Y. Chen, C. Luo, D. Liang, B. Hu, R. Qiu, K. Yan, *Appl. Catal. B.* **2020**, *277*, 119171.

[2] D. Kim, K. Yong, *Appl. Catal. B.* **2021**, *282*, 119538.

[3] S. Wang, B. Zhu, M. Liu, L. Zhang, J. Yu, M. Zhou, *Appl. Catal. B.* **2019**, *243*, 19.

[4] L. Carbone, A. Jakab, Y. Khalavka, C. Sönnichsen, *Nano Lett.* **2009**, *9*, 3710.

[5] C.-W. Tsao, M.-J. Fang, Y.-J. Hsu, *Coord. Chem. Rev.* **2021**, *438*, 213876.

[6] M.-J. Fang, C.-W. Tsao, Y.-J. Hsu, *J. Phys. D.* **2020**, *53*, 143001.

[7] S. Eustis, M. A. El-Sayed, *Chem. Soc. Rev.* **2006**, *35*, 209.

[8] Y.-C. Pu, G. Wang, K.-D. Chang, Y. Ling, Y.-K. Lin, B. C. Fitzmorris, C.-M. Liu, X. Lu, Y. Tong, J. Z. Zhang, Y.-J. Hsu, Y. Li, *Nano Lett.* **2013**, *13*, 3817.

[9] J.-M. Li, H.-Y. Cheng, Y.-H. Chiu, Y.-J. Hsu, *Nanoscale.* **2016**, *8*, 15720.

[10] Y.-H. Chiu, K.-D. Chang, Y.-J. Hsu, *J. Mater. Chem. A.* **2018**, *6*, 4286.

[11] M. A. Mahmoud, D. O'Neil, M. A. El-Sayed, *Chem. Mater.* **2014**, *26*, 44.

[12] A. Genç, J. Patarroyo, J. Sancho-Parramon, R. Arenal, M. Duchamp, E. E. Gonzalez, L. Henrard, N. G. Bastús, R. E. Dunin-Borkowski, V. F. Puntes, J. Arbiol, *ACS Photonics.* **2016**, *3*, 770.

[13] N. Halas, *MRS Bull.* **2005**, *30*, 362.

[14] S. A. Lindley, J. K. Cooper, M. D. Rojas-Andrade, V. Fung, C. J. Leahy, S. Chen, J. Z. Zhang, *ACS Appl. Mater. Interfaces.* **2018**, *10*, 12992.

[15] J. R. Daniel, L. A. McCarthy, E. Ringe, D. Boudreau, *RSC Adv.* **2019**, *9*, 389.

[16] B. Lu, A. Liu, H. Wu, Q. Shen, T. Zhao, J. Wang, *Langmuir.* **2016**, *32*, 3085.

[17] Y.-H. Chiu, S. A. Lindley, C.-W. Tsao, M.-Y. Kuo, J. K. Cooper, Y.-J. Hsu, J. Z. Zhang, *J. Phys. Chem. C* **2020**, *124*, 11333.

[18] S. Li, L. Wang, Y. Li, L. Zhang, A. Wang, N. Xiao, Y. Gao, N. Li, W. Song, L. Ge, J. Liu, *Appl. Catal. B.* **2019**, *254*, 145.

[19] W. Zhong, S. Shen, M. He, D. Wang, Z. Wang, Z. Lin, W. Tu, J. Yu, *Appl. Catal. B.* **2019**, *258*, 117967.

[20] Y.-H. Hsu, A. T. Nguyen, Y.-H. Chiu, J.-M. Li, Y.-J. Hsu, *Appl. Catal. B.* **2016**, *185*, 133.

[21] W.-H. Lin, Y.-H. Chiu, P.-W. Shao, Y.-J. Hsu, *ACS Appl. Mater. Interfaces.* **2016**, *8*, 32754.

[22] Y. Ju, H. Zhang, J. Yu, S. Tong, N. Tian, Z. Wang, X. Wang, X. Su, X. Chu, J. Lin, Y. Ding, G. Li, F. Sheng, Y. Hou, *ACS Nano.* **2017**, *11*, 9239.

[23] L. Liu, T. D. Dao, R. Kodiyath, Q. Kang, H. Abe, T. Nagao, J. Ye, *Adv. Funct. Mater.* **2014**, *24*, 7754.

[24] Y.-C. Pu, W.-T. Chen, M.-J. Fang, Y.-L. Chen, K.-A. Tsai, W.-H. Lin, Y.-J. Hsu, *J. Mater. Chem. A.* **2018**, *6*, 17503.

[25] M.-Y. Kuo, C.-F. Hsiao, Y.-H. Chiu, T.-H. Lai, M.-J. Fang, J.-Y. Wu, J.-W. Chen, C.-L. Wu, K.-H. Wei, H.-C. Lin, Y.-J. Hsu, *Appl. Catal. B.* **2019**, *242*, 499.

[26] J.-Y. Wu, T.-H. Lai, M.-J. Fang, J.-Y. Chen, M.-Y. Kuo, Y.-H. Chiu, P.-Y. Hsieh, C.-W. Tsao, H.-E. Chang, Y.-P. Chang, C.-Y. Wang, C.-Y. Chen, M. Sone, W.-W. Wu, T.-F. M. Chang, Y.-J. Hsu, *ACS Appl. Nano Mater.* **2022**, *5*, 8404.

[27] A. G. M. da Silva, T. S. Rodrigues, V. G. Correia, T. V. Alves, R. S. Alves, R. A. Ando, F. R. Ornellas, J. Wang, L. H. Andrade, P. H. C. Camargo, *Angew. Chem., Int. Ed.* **2016**, *55*, 7111.

[28] T.-H. Lai, C.-W. Tsao, M.-J. Fang, J.-Y. Wu, Y.-P. Chang, Y.-H. Chiu, P.-Y. Hsieh, M.-Y. Kuo, K.-D. Chang, Y.-J. Hsu, *ACS Appl. Mater. Interfaces.* **2022**, *14*, 40771.

[29] Y.-A. Chen, Y.-T. Wang, H. S. Moon, K. Yong, Y.-J. Hsu, *RSC Adv.* **2021**, *11*, 12288.

[30] T.-G. Vo, G.-S. Tran, C.-L. Chiang, Y.-G. Lin, H.-E. Chang, H.-H. Kuo, C.-Y. Chiang, Y.-J. Hsu, *Adv. Funct. Mater.* **2023**, *33*, 2370021.

[31] S. Yin, R. D. Kumar, H. Yu, C. Li, Z. Wang, Y. Xu, X. Li, L. Wang, H. Wang, *ACS Sustainable Chem. Eng.* **2019**, *7*, 14867.

[32] J. C. Park, H. Song, *Nano Res.* **2011**, *4*, 33.

[33] NOD Lab at NCTUMSE, Movement of the Au yolk inside the Cu7S4 shell for Au@Cu7S4 yolk-shell nanocrystals, YouTube, https://www.youtube.com/watch?v=_cgUeqesgDs, (accessed: February 2024).

[34] Z. W. Seh, S. Liu, M. Low, S.-Y. Zhang, Z. Liu, A. Mlayah, M.-Y. Han, *Adv. Mater.* **2012**, *24*, 2310.

[35] Y.-H. Chiu, S. B. Naghadeh, S. A. Lindley, T.-H. Lai, M.-Y. Kuo, K.-D. Chang, J. Z. Zhang, Y.-J. Hsu, *Nano Energy.* **2019**, *62*, 289.

[36] X. Zou, Y. Yang, H. Chen, X.-L. Shi, G. Suo, X. Ye, L. Zhang, X. Hou, L. Feng, Z.-G. Chen, *J. Colloid Interface Sci.* **2020**, *579*, 463.

[37] N. Wang, G. Cheng, L. Guo, B. Tan, S. Jin, *Adv. Funct. Mater.* **2019**, *29*, 1904781.

[38] H.-P. Liang, L.-J. Wan, C.-L. Bai, L. Jiang, *J. Phys. Chem. B.* **2005**, *109*, 7795.

[39] Y. Lu, Y. Zhao, L. Yu, L. Dong, C. Shi, M.-J. Hu, Y.-J. Xu, L.-P. Wen, S.-H. Yu, *Adv. Mater.* **2010**, *22*, 1407.

[40] K. An, T. Hyeon, *Nano Today.* **2009**, *4*, 359.

[41] H. Zhang, Z. Zhang, B. Li, Y. Hua, C. Wang, X. Zhao, X. Liu, *CrystEngComm.* **2015**, *17*, 3908.

[42] S. Jiao, L. Xu, K. Jiang, D. Xu, *Adv. Mater.* **2006**, *18*, 1174.

[43] S. Sun, S. Wang, D. Deng, Z. Yang, *New J. Chem.* **2013**, *37*, 3679.

[44] A. M. Schwartzberg, T. Y. Olson, C. E. Talley, J. Z. Zhang, *J. Phys. Chem. B.* **2006**, *110*, 19935.

[45] J. K. Young, N. A. Lewinski, R. J. Langsner, L. C. Kennedy, A. Satyanarayan, V. Nammalvar, A. Y. Lin, R. A. Drezek, *Nanoscale Res. Lett.* **2011**, *6*, 428.

[46] K. Senthil, D. Mangalaraj, S. K. Narayandass, S. Adachi, *Mater. Sci. Eng. B.* **2000**, *78*, 53.

[47] P. Mulvaney, L. M. Liz-Marzán, M. Giersig, T. Ung, *J. Mater. Chem.* **2000**, *10*, 1259.

[48] J. Zhao, S. Xue, R. Ji, B. Li, J. Li, *Chem. Soc. Rev.* **2021**, *50*, 12070.

[49] Y.-C. Lin, C.-K. Peng, S.-C. Lim, C.-L. Chen, T.-N. Nguyen, T.-T. Wang, M.-C. Lin, Y.-J. Hsu, S.-Y. Chen, Y.-G. Lin, *Appl. Catal. B.* **2021**, *285*, 119846.

[50] Y.-C. Lin, L.-C. Hsu, C.-Y. Lin, C.-L. Chiang, C.-M. Chou, W.-W. Wu, S.-Y. Chen, Y.-G. Lin, *ACS Appl. Mater. Interfaces.* **2019**, *11*, 38625.

[51] Y. Liu, L. Tan, G. Cibin, D. Gianolio, S. Han, K. Yu, M. T. Dove, A. V. Sapelkin, *Nanoscale.* **2020**, *12*, 19325.

[52] K. Hoffmann, I. Christl, R. Kaegi, R. Kretzschmar, *Environ. Sci. Nano.* **2020**, *7*, 3385.

[53] C. López-Cartes, T. C. Rojas, R. Litrán, D. Martínez-Martínez, J. M. de la Fuente, S. Penadés, A. Fernández, *J. Phys. Chem. B.* **2005**, *109*, 8761.

[54] K. Wu, H. Zhu, Z. Liu, W. Rodríguez-Córdoba, T. Lian, *J. Am. Chem. Soc.* **2012**, *134*, 10337.

[55] K. Wu, W. E. Rodríguez-Córdoba, Y. Yang, T. Lian, *Nano Lett.* **2013**, *13*, 5255.

[56] H. Li, S. Wang, J. Tang, H. Xie, J. Ma, H. Chi, C. Li, *Cell Rep. Phys. Sci.* **2023**, *4*, 101386.

[57] N. Zhou, H. Zhu, S. Li, J. Yang, T. Zhao, Y. Li, Q.-H. Xu, *J. Phys. Chem. C.* **2018**, *122*, 7824.

[58] H. Li, S. Wang, M. Wang, Y. Gao, J. Tang, S. Zhao, H. Chi, P. Zhang, J. Qu, F. Fan, C. Li, *Angew. Chem., Int. Ed.* **2022**, *61*, 202204272.

[59] Y. Gao, Q. Zhu, S. He, S. Wang, W. Nie, K. Wu, F. Fan, C. Li, *Nano Lett.* **2023**, *23*, 3540.

[60] H. Lee, D. Kim, *Opt. Express.* **2016**, *24*, 11994.

[61] M. S. Romero-Cano, B. Vincent, *J. Controlled Release.* **2002**, *82*, 127.

[62] P.-Y. Hsieh, T. Kameyama, T. Takiyama, K. Masuoka, T. Yamamoto, Y.-J. Hsu, T. Torimoto, *J. Mater. Chem. A.* **2020**, *8*, 13142.

[63] M. L. Brongersma, N. J. Halas, P. Nordlander, *Nat. Nanotechnol.* **2015**, *10*, 25.

[64] A. Kumar, P. Choudhary, A. Kumar, P. H. C. Camargo, V. Krishnan, *Small.* **2022**, *18*, 2101638.

[65] W. Li, Y. Dang, T. Ma, J. Li, G. Liao, F. Gao, W. Duan, X. Wang, C. Wang, *Sol. RRL.* **2023**, *7*, 2300110.

[66] K. Cai, W. Zhang, J. Zhang, H. Li, H. Han, T. Zhai, *ACS Appl. Mater. Interfaces.* **2018**, *10*, 36703.

[67] W. Li, S. Xie, M. Li, X. Ouyang, G. Cui, X. Lu, Y. Tong, *J. Mater. Chem. A.* **2013**, *1*, 4190.

[68] C. Wang, L. Wang, J. Jin, J. Liu, Y. Li, M. Wu, L. Chen, B. Wang, X. Yang, B.-L. Su, *Appl. Catal. B.* **2016**, *188*, 351.

[69] L. Wei, Z. Guo, X. Jia, *Catal. Lett.* **2021**, *151*, 56.

[70] J. K. Nørskov, T. Bligaard, A. Logadottir, J. R. Kitchin, J. G. Chen, S. Pandelov, U. Stimming, *J. Electrochem. Soc.* **2005**, *152*, J23.

[71] Y.-C. Pu, W.-H. Lin, Y.-J. Hsu, *Appl. Catal. B.* **2015**, *163*, 343.

[72] J.-P. Chang, C.-Y. Wang, Y.-J. Hsu, C.-Y. Wang, *Appl. Catal. A: Gen.* **2023**, *650*, 119005.

[73] Y.-C. Pu, F. Song, W. Zhang, S. Lindley, S. Adams, J. Z. Zhang, *Part. Part. Syst. Charact.* **2017**, *34*, 1600255.

[74] I. Hong, Y.-A. Chen, Y.-J. Hsu, K. Yong, *ACS Appl. Mater. Interfaces.* **2021**, *13*, 52670.

[75] G. Kresse, J. Furthmüller, *Phys. Rev. B.* **1996**, *54*, 11169.

[76] G. Kresse, J. Furthmüller, *Comput. Mater. Sci.* **1996**, *6*, 15.

[77] P. E. Blöchl, *Phys. Rev. B.* **1994**, *50*, 17953.

[78] J. P. Perdew, K. Burke, M. Ernzerhof, *Phys. Rev. Lett.* **1996**, *77*, 3865.

[79] J. P. Perdew, K. Burke, Y. Wang, *Phys. Rev. B.* **1996**, *54*, 16533.

[80] G. Henkelman, A. Arnaldsson, H. Jónsson, *Comput. Mater. Sci.* **2006**, *36*, 354.

[81] R. F. W. Bader, *Atoms in Molecules: A Quantum Theory*, Oxford University Press, Oxford, ENG UK **1994**.

[82] T. Liao, L. Kou, A. Du, Y. Gu, Z. Sun, *J. Am. Chem. Soc.* **2018**, *140*, 9159.

[83] H. Li, S. Dai, D. Bhalothia, A. Hu, J.-P. Chou, T.-Y. Chen, *J. Mater. Chem. A.* **2021**, *9*, 12019.

[84] M. Chase, *NIST-JANAF Thermochemical Tables*, American Institute of Physics, College Park, MD, USA **1998**.